



UNIVERSIDADE FEDERAL DE
CAMPINA GRANDE

aa/bb/cc/dd-TDI

**OBSERVAÇÕES DE LONGO PRAZO DE ONDAS DE
GRAVIDADE DE MÉDIA ESCALA SOBRE A REGIÃO
EQUATORIAL BRASILEIRA**

Patrick Essien

Dissertação de Mestrado do Curso de Pós-Graduação em Física da Atmosfera Superior, orientada pelos Doutores Igo Paulino, Amauri Fragoso de Medeiros.

UFCG
Campina Grande
2015

PUBLICADO POR:

UNIVERSIDADE FEDERAL DE CAMPINA GRANDE - UFCG

Centro de Ciências e Tecnologia

Unidade Acadêmica de Física

Programa de Pós Graduação em Física

Rua Aprígio Veloso, 882. Bairro Universitário

Campina Grande - PB - Brasil

Tel.:(083) 2101-1195/1060

E-mail: pgfisica@df.ufcg.edu.br

**CONSELHO DE EDITORAÇÃO E PRESERVAÇÃO DA PRODUÇÃO
INTELECTUAL DA UAF/CCT/UFCG:**

Presidente:

Prof. Dr. Igo Paulino (UAF)

Membros:

Prof. Dr. Amauri Fragoso de Medeiros (UAF)

Prof. Dr. Ricardo Arlen Buriti (UAF)

BIBLIOTECA DIGITAL:

Prof. Dr. Igo Paulino (UAF)

REVISÃO E NORMALIZAÇÃO DOCUMENTÁRIA:

Prof. Dr. Amauri Fragoso de Medeiros (UAF)

Prof. Dr. Ricardo Arlen Buriti (UAF)

EDITORAÇÃO ELETRÔNICA:

Prof. Dr. Igo Paulino (UAF)



UNIVERSIDADE FEDERAL DE
CAMPINA GRANDE

aa/bb/cc/dd-TDI

**OBSERVAÇÕES DE LONGO PRAZO DE ONDAS DE
GRAVIDADE DE MÉDIA ESCALA SOBRE A REGIÃO
EQUATORIAL BRASILEIRA**

Patrick Essien

Dissertação de Mestrado do Curso de Pós-Graduação em Física da Atmosfera Superior, orientada pelos Doutores Igo Paulino, Amauri Fragoso de Medeiros.

UFCG
Campina Grande
2015

E78o Essien, Patrick.
 Observações de longo prazo de ondas de gravidade de média escala sobre a região equatorial brasileira / Patrick Essien. – Campina Grande, 2015.
 65 f. : il. color.

 Dissertação (Mestrado em Física) – Universidade Federal de Campina Grande, Centro de Ciências e Tecnologia, 2015.
 "Orientação: Prof. Dr. Igo Paulino, Prof. Dr. Amauri Fragoso de Medeiros".
 Referências.

 1. Aeroluminescência. 2. Onda de Gravidade. 3. Keogram. 4. Vento Neutro. I. Paulino, Igo. II. Medeiros, Amauri Fragoso de. III. Título.

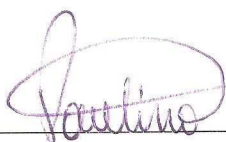
CDU 551.511.31(043)

PATRICK ESSIEN

**OBSERVAÇÕES DE ONDAS DE GRAVIDADE NA REGIÃO EQUATORIAL
BRASILEIRA DURANTE O CICLO SOLAR 24**

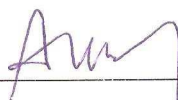
Dissertação aprovada em 03/12/2015

BANCA EXAMINADORA



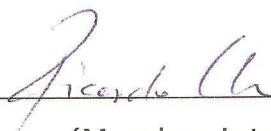
(Presidente)

Prof. Dr. Igo Paulino da Silva
Unidade Acadêmica de Física – UFCG



(Co-Orientador)

Prof. Dr. Amauri Fragoso de Medeiros
Unidade Acadêmica de Física – UFCG



(Membro interno)

Prof. Dr. Ricardo Arlen Buriti da Costa
Unidade Acadêmica de Física – UFCG



(Membro externo)

Prof. Dr. Ricardo Yvan de la Cruz Cueva
Departamento de Física - UEMA

Dados Internacionais de Catalogação na Publicação (CIP)

Essien, Patrick.

Cutter Observações de longo prazo de ondas de gravidade de média escala sobre a região equatorial brasileira / Patrick Essien. – Campina Grande : UFCG, 2015.

xxi + 65 p. ; (aa/bb/cc/dd-TDI)

Dissertação (Mestrado em Física) – Universidade Federal de Campina Grande, Campina Grande, 2012.

Orientadores : Igo Paulino e Amauri Fragoso de Medeiros.

1. Aeroluminescência. 2. Onda de gravidade 3. Keogram.
4. Vento neutro. I. Título.

CDU 000.000

Copyright © 2015 da UAF/CCT/UFCG. Nenhuma parte desta publicação pode ser reproduzida, armazenada em um sistema de recuperação, ou transmitida sob qualquer forma ou por qualquer meio, eletrônico, mecânico, fotográfico, reprográfico, de microfilmagem ou outros, sem a permissão escrita da UFCG, com exceção de qualquer material fornecido especificamente com o propósito de ser entrado e executado num sistema computacional, para o uso exclusivo do leitor da obra.

Copyright © 2015 by UAF/CCT/UFCG. No part of this publication may be reproduced, stored in a retrieval system, or transmitted in any form or by any means, electronic, mechanical, photocopying, recording, microfilming, or otherwise, without written permission from UFCG, with the exception of any material supplied specifically for the purpose of being entered and executed on a computer system, for exclusive use of the reader of the work.

**ATENÇÃO! A FOLHA DE
APROVAÇÃO SERÁ IN-
CLUIDA POSTERIORMENTE.**

Mestrado em Física

Man must rise above the Earth to the top of the atmosphere and beyond for only thus will he fully understand the world in which he lives

SOCRATES
“An Ancient Greek Philosopher”, (469-399 BC)

I dedicate this dissertation to **Prof. Dr. Igo Paulino, Dr. Mrs. Ana Reberta Paulino, Prof. Dr. Ricard Buriti and Prof. Dr. M. Amauri**

AGRADECIMENTOS

The quality of a person's life is in direct proportion to their commitment to excellence regardless of chosen fields of endeavor. I do preface this citation in the honor of Prof. Dr. Igo Paulino, knowing very well the immense contributions made and services rendered to bring this research to success. Your efforts of advancing the course are still fresh in my mind and I have no other option than to show appreciation and gratitude for your extraordinary support.

This affirms what Martin Luther King Jnr said that, *Life's most persistent and urgent question is what you are doing for others*. Better still, the core concern you devoted for me throughout my post graduation program, also affirms that, *People don't care how much you know until they know how much you care provided you have done more than enough*. And explicitly, you have done more than expected of every potential Leader. To acknowledge your effort is not enough; to be grateful for your support is not enough, but to learn hard, continue the good works you have started in me and apply what I have learned would go a long way to add more glory to your credibility.

I would also like to express my deepest gratitude to Prof. Dr, Ricard Buriti and Prof. Dr. Amauri, for their excellent guidance, caring, patience, and providing me with an excellent atmosphere for doing research. I would like to thank all my friends for the motivation and all support they offered.

LONG-TERM OBSERVATION OF MEDIUM SCALE GRAVITY WAVES OVER BRAZILIAN EQUATORIAL REGION

ABSTRACT

This project has studied the long term observations of medium-scale gravity waves over Brazilian equatorial region. As part of this objective, 11 years (2000 to 2010) all-sky image measurements of mesospheric gravity waves were made successfully from Sao Joao do Cariri (7.40°S, 36.50°W) of the magnetic equator. The long term observation provided continuous measurements of the medium scale-gravity waves characteristic structures to be analyzed. Keograms analysis was used to determine the parameters of 537 medium-scale gravity waves observed in the OH emission at ~ 87 km altitude. The characteristics were studied as well as the seasonality of the phase propagation direction, and the evolution of the MSGWs according to the solar cycle. The maximum horizontal wavelength, observed period and the phase speed were concentrated between 100 to 150 km, 20 to 40 m/s and 60 to 80 minutes, respectively. The total anisotropy of the propagation direction were preference to Northeast of the site and was more significant during Spring and Summer seasons, however autumn and winter were evenly propagated. The critical layer theory for gravity wave filtering was applied to 2003 dataset to study the effects of middle atmospheric winds on the propagation of medium-scale gravity waves. And it was found that these waves were less susceptible to wind filtering effects especially during summer season. It was also observed that some of the medium-scale were capable of propagating into the lower thermosphere where they may have acted directly as seeds for the Rayleigh-Taylor instability development. There was no direct correlation between the evolution of the MSGWs and the solar cycle activity, therefore, it can be concluded that, the wave events were primarily generated in Brazil equatorial region by meteorological processes. Finally, it was affirmed that keogram methodology appear as a good tool to study the spectral characteristics of MSGWs in the MLT since the results are in consistence with the literature.

LISTA DE FIGURAS

	<u>Pág.</u>
2.1 Vertical structure of the atmosphere-ionosphere system, where the neutral atmospheric temperature.	8
2.2 Atmospheric Gravity waves are the oscillations of air parcels by the lifting force of bouyancy	11
2.3 AGWs generated at the lower ionosphere by the acoustic wave launched at the sea surface around the tsunami.	13
2.4 Four images showing examples of gravity wave structure recorded in the OI(557.7 nm) and near-infrared OH emissions during the campaign:(a, b) extensive bands; (c) example of transient ripples; (d) a complex mixture of band and ripple waves. Note that the oval silhouette at the bottom of each image is the Instituto Nacional de Pesquisas Espaciais satellite tracking antenna, while the dark patches at low elevations in (b) and (c) are clouds ??)	15
2.5 Example west-east Keograms for (a) Cariri and (b) Brasilia obtained on the night of 1-2 October. The medium-scale gravity waves appear as coherent, tilted bands. ??)	17
2.6 Keogram of the flatfield images of OI 6300 (top) and OHNIR (bottom) at Cariri on 30 September 2005: N-S cut (leftside) and EW cut (rightside). 18	
3.1 Lens mechanics and optical diagram of all-sky lens	28
3.2 The All Sky Imaging System: source??)	30
3.3 The projection of the observation site, Sao Joao do Cariri	32
3.4 Images observed by the all sky imager in Cariri	33
3.5 Preprocessing of the images. (a) OH image observed from the night of 1st to 2nd September, 2002 in Sao Joao do Cariri. (b) after the stars were removed. The white lines cut through the image exactly in the center (c) linear image. Note that the white lines shown in (b) appear to be rotated and shifted to the center due to the conversion process to the geographical coordinates. The black lines indicate the true north-south direction (vertical) and east-west (horizontal).source;	34
3.6 Sequence of images showing simulated propagation of medium-scale gravity waves to the northwest. The white lines represent the regions where the zonal and meridional cuts are made for the construction of Keograms	36

3.7	Keogram constructed from the images of the sequence shown in Figure 3.3.2. (a) meridional and (b) zonal, components	38
3.8	The Line of best fit for the correlation analysis of a keogram for the estimation of the horizontal parameters	39
3.9	The estimation of the phase propagation direction using the slope of the line of best fit.	40
3.10	The projection of OH NIR airglow image area	43
4.1	The histogram distribution of the (a) observed periods of propagation (b) horizontal wavelengths of (c) phase speed; of the MSGWs that were observed in Sao Joa do Cariri from the year 2000 to 2010	46
4.2	The seasonality of the propagation direction of the MSGWs	50
4.3	The total number of MSGWs observed as a function of the Months (The colors represent the propagation direction)	51
4.4	Three-dimensional blocking diagram from 0 to 98Km for the 4 seasons in the year 2003	55
4.5	Blocking diagram the four seasons showing the OH layer at height 86 km. The arrows indicate the magnitudes and directions of the phase velocity of the waves during each season	56
4.6	The evolution of the MSGWs according to the solar cycle (i.e. Solar flux F10.7)	58

LISTA DE TABELAS

	<u>Pág.</u>
2.1 Typical temporal scales of internal waves in the terrestrial atmosphere, source; (??)	9
3.1 Filter Information and Mean Heights for Airglow Emissions in Upper Mesosphere, Source; (??)	31
3.2 The approximate propagation direction of GWs obtained from the visualization of keograms. incr indicates increasing profile phase, 'decr' decreasing profile phase and 'const' constant profile phase.	41

LISTA DE ABREVIATURAS E SIGLAS

AGWs	– Atmospheric Gravity Waves
GWs	– Gravity Waves
MLT	– Método das Covariâncias
MSGWs	– Medium-Scale Gravity Waves
FFT	– Fast Fourier Transform
SSGWs	– Medium-Scale Gravity Waves
LSGWs	– Large Scale Gravity Waves
ASI	– All Sky Imager
SABER	– Sounding of the Atmosphere using Broadband Emission Radiometry
TIMED	– Thermosphere Ionosphere Mesosphere Energetics and Dynamics
MLTI	– Mesosphere and Lower Thermosphere/Ionosphere
CCD	– Charge Coupled Device
GUVI	– Global Ultraviolet Imager
TIDI	– TIMED Doppler Interferometer
SEE	– Solar Extreme-Ultraviolet Experiment
1-D	– one-dimensional
2-D	– two-dimensional
3-D	– three-dimensional
UFCG	– Universidade Federal de Campina Grande
OH	– Hydroxide
NIR	– Near Infra-Red
EUV	– Extreme Ultraviolet
RTI	– Rayleigh-Taylor Instability
ALOHA	– Airborne Lidar and Observations of the Hawaiian Airglow
SpreadFEx	– Equatorial Spread F
CP	– Cachoeira Paulista
TJS	– Tanjungsari
EPB	– Equatorial Plasma Bubbles
CHAMP	– Challenging Minisatellite Payload
LF	– Low Frequency
TID	– Traveling Ionospheric Disturbances
QBO	– Quasi Biennial Oscillation
TI	– Thermosphere-Ionosphere
LCTFs	– Liquid Crystal Tunable Filters
CRi	– Cambridge Research and Instrumentation
EMCCD	– Electron Multiplying Charge Coupled Device
IDL	– Interactive Data Language

LISTA DE SÍMBOLOS

a	–	primeira contante
b	–	segunda constante
ρ	–	densidade de um fluido
ν	–	viscosidade cinemática
Re	–	número de Reynolds
α	–	constante de Kolmogorov
k	–	número de onda
K	–	curtose
D_0	–	dimensão de contagem de caixas
D_1	–	dimensão de informação
D_2	–	dimensão de correlação
λ_1	–	expoente de Lyapunov dominante

SUMÁRIO

	<u>Pág.</u>
1 INTRODUCTION	1
1.1 Motivation	1
1.2 Objectives os the Research	4
1.3 Structure of the Dessertation	4
2 Literature Review of Atmospheric Gravity Waves and Equation of Waves	7
2.1 The structure and dynamics of the Earth’s atmosphere	7
2.2 Internal Waves Characteristics	9
2.3 Review of Atmospheric Gravity Waves	14
2.4 Linear Theory	20
2.4.1 Equation of Motion	20
3 Instrumentation and Methodology	27
3.1 The All Sky Imager	27
3.2 Period of observation and study area	31
3.3 Determination of Gravity Wave Parameters	33
3.3.1 Pre-processing of the airglow images	33
3.3.2 Method of Keogram Analysis	35
4 Results and Discussion	45
4.1 Parameters of Medium Scale Gravity Waves	45
4.1.1 The horizontal; Wavelength, period and phase speed	45
4.1.2 Phase Propagation direction and Seasonality of Medium Scale Gravity Waves	49
4.1.3 The parameters of MSGWs and solar cycle	57
5 Conclusion and Recommendation	61
5.1 Conclusion	61
5.2 Recommendation	62

1 INTRODUCTION

In fluid dynamics, gravity waves are waves generated in a fluid medium or at the interface between two media (e.g. the atmosphere and the ocean) which has the restoring force of gravity or buoyancy. When a fluid element is displaced on an interface or internally to a region with a different density, gravity tries to restore the parcel toward equilibrium resulting in an oscillation about the equilibrium state or wave orbit. Gravity waves on an air-sea interface are called surface gravity waves or surface waves while internal gravity waves are called internal waves. Atmospheric gravity waves is a typical example of internal gravity that are normally generated through the process of vertical movement of air-parcel forced by convections, front activity and topography in the troposphere and wind shear instability in the whole atmosphere, (??????). It is produced under a balance of the buoyancy and gravity forces. Once the oscillation is generated, it propagates horizontally and vertically transporting energy and momentum. As a result, the wind, density and temperature fields are perturbed. The amplitudes of these oscillations increase exponentially with height because of the exponential decrease of the atmospheric density and are known to play a key role in the MLT dynamics, e.g. (????????????).

1.1 Motivation

About a decade ago, many scientists regarded AGWs as simply idle curiosities which was considered that they had no real impact on atmospheric motions or dynamics at any sort of important scale. However recent research had recognized that GWs are the main mechanism that carry momentum and energy between different points in the atmosphere. This implies that if a gravity wave is generated at a source region and dissipates somewhere else, it amounts to a transfer of energy and momentum from the first point to the other. Moreover, the energy and momentum deposited can alter the mean flow in that region. Meteorologists have realized in the last decade that computer models are not always very good at predicting mean winds, or making accurate forecasts, and have discovered that it was the absence of gravity wave generation and dissipation in their models, e.g (??). A considerable amount of effort has turned towards proper parametrization of gravity waves in meteorological models since GWs were considered as an important physical process in the climate and forecast meteorological models. For instance, in the mesosphere it has been found that by including gravity waves in meteorological models, the directions of the winds have in some cases reversed relative to the expected wind directions deduced without

inclusion of gravity waves. The values deduced with gravity waves included in the models agree better with observations than do the older predictions according to ??).

Many work have been done in the Brazil equatorial region by ??????????) but all these studies were conducted within a short period, however this work, this work is a study of 11 years data of medium-scale gravity waves which is the longest period of study ever in this equatorial region. These dataset provides important information for the study of the long term characteristics of the medium-scale gravity wave events. This wave events is very significant in the atmospheric/ionospheric dynamics and even ??) modeling studies have shown that a significant fraction of the convectively generated gravity waves of medium-scales with horizontal wavelength ($\lambda_x > 100$ km and observed periods of a few tens of minutes) are capable of propagating well into the lower thermosphere where they may directly act as seeds for the Rayleigh-Taylor Instability (RTI). It is also possible to cause This equatorial spreadFex (ESF) irregularities which have been studied intensively during the two consecutive SpreadFEx campaign in Brazil equatorial region by (?????????), because of their importance in understanding thermosphere-ionosphere coupling and their detrimental influence on radio communications. ESF has been shown to create significant errors in GPS position measurements at low-latitudes when the line-of-sight satellite signals pass through strong equatorial plasma bubbles (EPB) also termed depletions, (????).

These waves are readily observed at mesospheric heights using the naturally occurring airglow emission. The condition of vertical propagation and dissipation of the waves depends on the wave characteristics (wavelength and phase velocity) and the filtering by the background wind system. From ??), in the equatorial mesopause region (80 to 100 km), the gravity waves with a period of 5 to 30 min, horizontal wavelength of 10 to 100 km, phase velocity of 20-80 m/s, are frequently observed by airglow imaging system, which are known to contribute significantly to momentum deposition at MLT heights. Some of these waves have a condition to propagate above 100 km, even up to 200 km in the ionosphere according to ??). However, ??) made it emphatically that when gravity waves propagates into the thermosphere, they are damping due to molecular viscosity and thermal diffusivity.

The naturally occurring nightglow emissions provide an important capability for remote measurements of gravity waves, especially, in the vicinity of the mesopause. ??)

demonstrated that most imaging studies have used the bright near infrared hydroxyl OH emission which originates from a well defined layer centered at ~ 87 km with a typical half-width of ~ 8 km. ??) affirmed that, as gravity waves propagates through this layer, it modulates the line-of-sight of the atmospheric fields and airglow emission, which appears as coherent wave structure in sensitive all-sky imaging systems ?????????????). Moreover, most of the time, these waves appear near linear; however on occasions well-defined concentric rings of GWs are detected over or near severe thunderstorms (????????????).

On the other hand, the propagation paths of convectively generated, high-frequency GWs with medium-scale horizontal wavelengths are much less sensitive to uncertainties in the horizontal winds in MLT, because their horizontal phase speeds are larger than for small-scale GWs. Since the useful field of view of all-sky measurements is typically 600 km at the OH emission height, GWs with medium-scale horizontal wavelengths of 60-500 km can also be detected at the same time as the shorter-scale waves which tend to dominate the image structure. Such measurements are usually also accompanied by background images to account for any contamination by meteorological clouds. Medium-scale GWs with brightness amplitudes of several percent are easily detected in the OH layer. According to ??), these waves are generally believed to be excited at or near the tropopause or lower stratosphere from processes such as convection, air flow over mountains, and geostrophic adjustment, rather than from wave breaking near the mesopause, which mostly creates small-scale, secondary GWs.

The medium-scale waves have broad range of scales from small-scale acoustic-gravity waves to large-scale inertia-gravity waves. At the mid-latitudes, the periods of gravity waves vary from several minutes to about 1 day. They are routinely seen in lidar, radar, airglow, and satellite measurements. For instance various investigations into the excitation, propagation, and decay of atmospheric gravity waves have been conducted through ground-based observations and satellite measurements by ?????). The medium-scale and secondary GWs are normally excited near the mesopause from the localized deposition of momentum which occurs during wave-breaking by ??), however, the amplitudes of these waves are only a few percent of the original breaking wave's amplitude, and are therefore less-likely to be detected in the OH layer. ??) suggested that when there are significant wind uncertainties, reverse ray tracing medium-scale GWs from the OH layer likely yields a more accurate identifi-

cation and quantification of their sources than reverse ray tracing small-scale GWs from the OH layer, because their phase speeds tend to be larger in general. However, a significant drawback is that medium-scale GWs are much less frequently observed than small scale GWs.

1.2 Objectives os the Research

The role of the lower atmospheric activities (gravity waves, tides and winds) in Brazil equitorial region have been fully discussed. Especially, the two consecutives SpreadFEx campaigns in 2005 and 2009 contributed to the increasing number of studies of GWs in the Mesosphere and Lower Thermosphere near the magnetic equator over Brazil (??????). However, no work has been reported on the long term study of the characteristics of gravity wave events in the MLT over Brazillian equatorial region and also whether or not any solar activity has influence on these wave events. For this purpose, MSGWs in OHNIR airglow emissions had been carried out from 2000 to 2010 by all-sky imager situated at Sao Joao do Cariri (7.40°S, 36.50°W). Therefore, the objectives of this work is;

- To study the characteristics of the MSGWs close proximity to the magnetic equator where thermospheric bubbles form and grow.
- To study the seansonality of the phase propagation direction
- To study the evolution of the MSGWs according to the solar cycle.

The later will address the question of how variations of solar activities influence the gravity wave events in the MLT, using solar flux F10.7cm.

1.3 Structure of the Dessertation

Capítulo 1 begins by introducing the general concept of atmospheric gravity waves and categorised them according to their parametric scales and also specifies the objectives of this study. In Capítulo 2, the basic concept of GWs will be discussed and proceeded with the review of the literature of the gravity waves and the Linear theory of Motion. Moreover, Capítulo 3 focuses on the instrumentation and the data analysis of the MSGWs. The analysis will adopt Keogram FFT technique to analyze the parameters and other related characteristics of MSGWs. Detail results

and discussions will be presented in [Capítulo 4](#). Finally, the conclusion based on the results and recommendation for future works will be dealt with in [Capítulo 5](#).

2 Literature Review of Atmospheric Gravity Waves and Equation of Waves

2.1 The structure and dynamics of the Earth's atmosphere

The structure and dynamics of the Earth's atmosphere are determined by a complex interplay of radiative, dynamical, thermal, chemical, and electrodynamic processes in the presence of solar and geomagnetic activity variations. The lower atmospheric processes are the primary concern of meteorology, while impacts of the Sun and geomagnetic processes on the atmosphere-ionosphere are the subject of space weather research as shown in [Figura 2.1](#). Thus, the whole atmosphere as a system is under the continuous influence of meteorological effects and space weather according to ??).

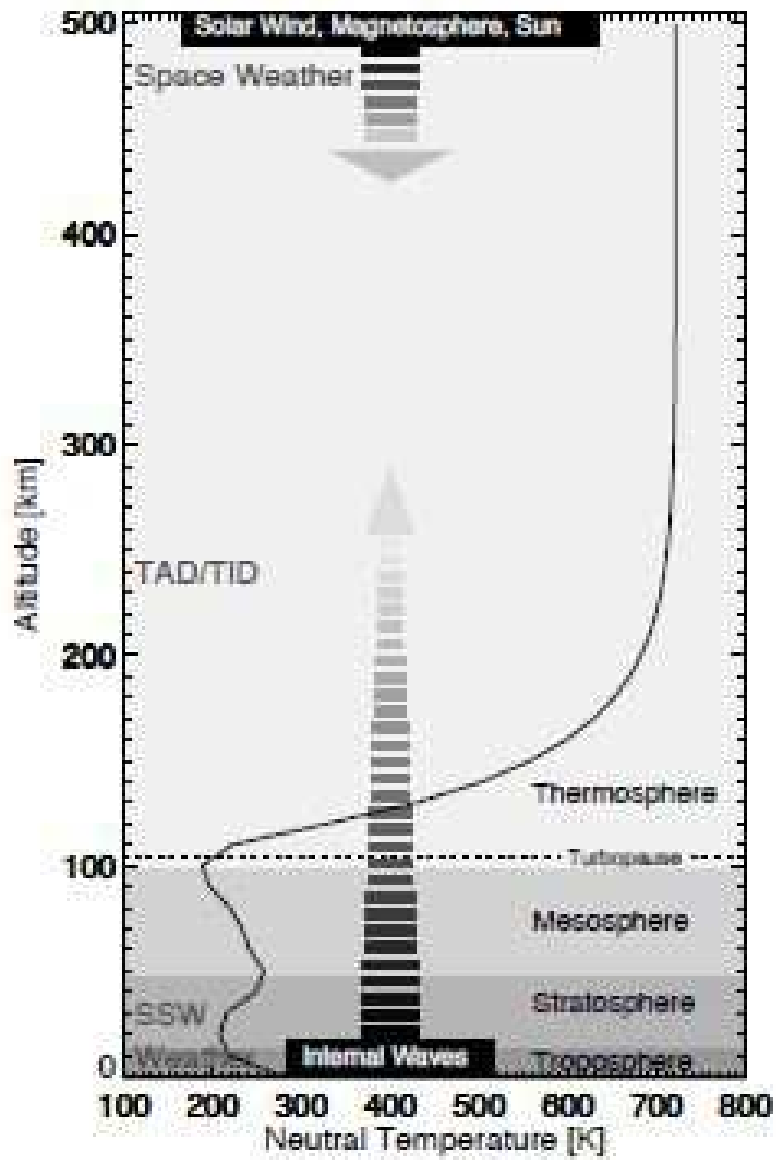


Figura 2.1 - Vertical structure of the atmosphere-ionosphere system, where the neutral atmospheric temperature.

Fonte: (??).

The atmosphere can be viewed as an ideal geophysical fluid that is pervaded by waves of various spatio-temporal scales. The term internal waves signifies the ability of waves to propagate vertically upward within the atmosphere, unlike external modes, in which all layers oscillate in synchrony when disturbances propagate horizontally. Internal waves exist because Earth's atmosphere is overall stably stratified. Horizontal scales of internal waves vary from a few kilometers to the planetary circumference. Temporal scales cover a range from minutes to several days. Internal waves can propagate over large distances, and transfer momentum and energy from lower levels to much higher altitudes, thus providing an important coupling mechanism in the atmosphere.

2.2 Internal Waves Characteristics

Approximately, atmospheric waves can be distinguished by their spatial scales. Earth's atmosphere possesses a broad spectrum of waves ranging from very small- (e.g., gravity waves, GWs) to planetary-scale waves (tides, Rossby waves). Table 2.1 summarizes quantitatively the range of temporal scales for tides, gravity, planetary Rossby and Kelvin waves. Overall, internal wave periods vary from few minutes to tens of days and also have different spatial scales. While small-scale GWs have typical horizontal wavelengths λ_H of several km to several hundred km, for instance horizontal scales of solar tides and planetary waves are comparable to the circumference of Earth.

Tabela 2.1 - Typical temporal scales of internal waves in the terrestrial atmosphere, source; (??)

Internal Wave	Typical range of temporal scales
Gravity wave	few minutes to several hours ($2\pi/f$, $f = 2\Omega \sin\phi$)
Solar tides	1, 1/2, 1/3, days
Planetary waves	2 to few tens of days
Kelvin waves	3 to 20 days

Although various internal waves can be excited by different mechanisms, in general, meteorological processes are the primary sources of these motions. GWs propagate upward and grow in amplitude due to exponentially decreasing neutral mass density ρ (in order to satisfy wave action conservation). Therefore, though wave disturbances associated with small-scale GWs are relatively small at the source levels, their

amplitudes can become significant at higher altitudes in the thermosphere, and are subjected to various dissipative processes. On the other hand, large-scale waves, such as planetary waves, can possess relatively larger amplitudes in the lower atmosphere, and dissipate at lower altitudes. This wave dissipation is the main mechanism of transfer of momentum and energy from disturbances to the mean flow.

Atmospheric Gravity waves are the oscillations of air parcels by restoring force of gravity which propagate vertically as shown in the [Figura 2.2](#), and actively transport energy and momentum from the troposphere to the middle and upper atmosphere. These exist in all types of geophysical fluids, such as lakes, oceans, and atmospheres, and play an important role in redistributing energy at disturbances, such as mountains or sea-mounts and are very important physical processes in meteorology and oceanography, particularly simulation models, atmospheric weather models, turbulence, air pollution, and climate research. Atmospheric Gravity Waves provides the working background of the fundamental physics and mathematics of gravity waves, and introduces a wide variety of applications in numerous recent advances. They are found to affect atmospheric tides in the middle atmosphere and terrestrial weather in the lower atmosphere. As these waves propagate upward, they play an important role in the atmospheric circulation at altitudes near the tropopause, and well above in the stratosphere and mesosphere.

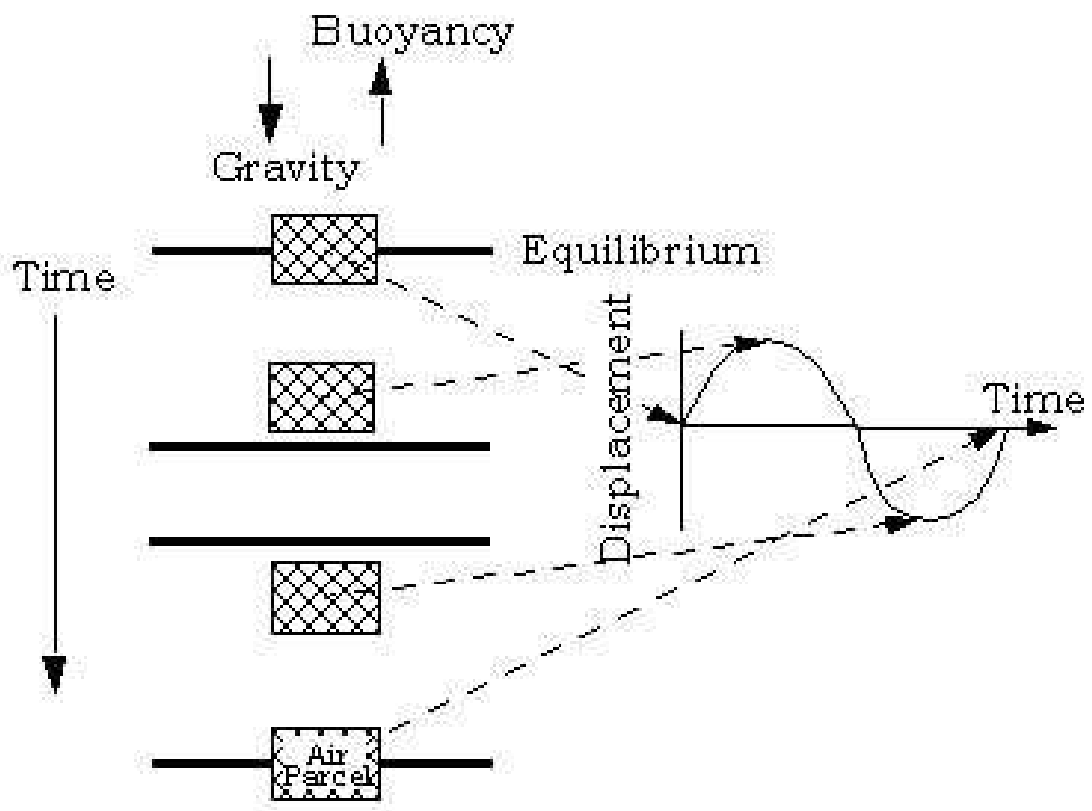


Figura 2.2 - Atmospheric Gravity waves are the oscillations of air parcels by the lifting force of buoyancy

Gravity waves significantly impact the global circulation pattern, thermal structures, and advective and diffusive transport of constituents, especially in the middle and upper atmospheres. For example, they are important or even the dominant driver of the quasi-biennial oscillation and semiannual oscillation in the equatorial stratosphere and mesosphere, and they also drive the mesosphere and lower thermosphere (MLT) circulation off radiative equilibrium in the summer and winter hemispheres (??) (for an extensive review of GW effects in the middle atmosphere). GW impact can extend into the thermosphere and ionosphere (TI). Turbulence induced by GW instability is likely to contribute to the exchange of mass around the turbopause and modifies the TI compositional structure and density, e.g. (??). According to (???) dissipation of GW can excite secondary GWs, which can also cause large TI perturbations. GWs breaking can also impact the MLT and TI dynamics by affecting the amplitude and phase of planetary waves and tidal waves, e.g. (??). From (??) gravity waves are also thought to cause the ionospheric sporadic E layer and the equatorial spread F (ESF) (??) and references there in, two ionospheric irregularities that alter the plasma densities and have important implications for space weather applications.

According to (??), unlike in the middle atmosphere, propagation of GWs in the TI is strongly influenced by dissipation. The latter is mainly due to molecular viscosity and heat conduction, but ion-friction caused by the interaction of the ionized atmosphere with the neutral flow is also a significant source of wave dissipation. Changes in the solar radiation absorption do not affect the dynamics of wave propagation directly. Instead, they modify the thermospheric temperature and winds, and thus, alter the density, static stability, dissipation, and refractive properties associated with the Doppler shift by the mean wind. Propagation of GWs in the dissipative thermosphere as well as their possible effects in the TI have been studied theoretically and numerically. However, insights into the links between the changes in the thermosphere driven by the solar radiation and GW responses remain very limited. The mean winds in the real atmosphere are generally non-zero and highly variable (??). They impact the propagation and dissipation of GWs significantly by altering their dispersion relation, and thus, the refractive properties. It is seen from that the modulation of the mean atmospheric state induced by variable solar radiation absorption enter the GW scheme via temperature dependence and of other dissipation coefficients.

It is considered that the first ionospheric concentric wave with the propagation velocity of about 3.5 km/s was caused by the acoustic wave generated from the propagating Rayleigh wave. The second and following concentric waves would correspond to the atmospheric gravity waves (AGW) propagating in the ionosphere. A typical example of AGWs that could be generated mainly at the lower ionosphere by the acoustic wave launched at the sea surface around the tsunami source as shown in Figura 2.3

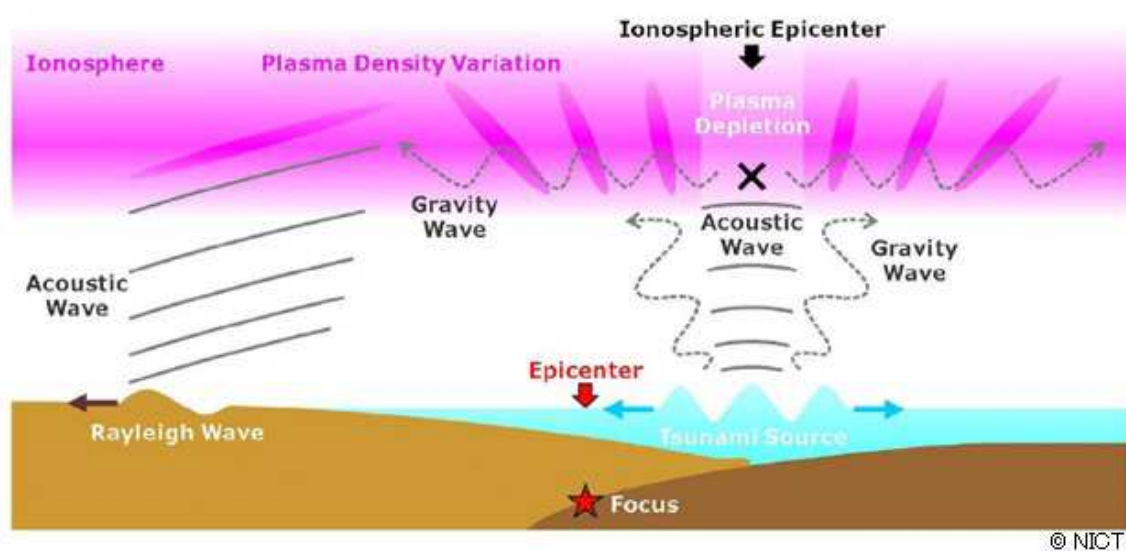


Figura 2.3 - AGWs generated at the lower ionosphere by the acoustic wave launched at the sea surface around the tsunami.

Fonte: <http://www.nict.go.jp/en/press/2011/30-01.html>

2.3 Review of Atmospheric Gravity Waves

Airglow observations have been made before 1950s and are useful to study morphology and dynamics of the MLT. The fundamental understanding of the gravity waves was provided by (??), who also derived the dispersion relation between frequency and the vertical and horizontal wavelengths as shown in the Equation 2.24. Indeed, the interest in the field continues to expand as many effects of gravity waves become better understood. From earlier photometric observations, it was found that there were periodic variations of the emission rates suggesting the presence of wave-like motions of the atmosphere. As a result of the advances in the airglow observation techniques, (??) carried out the first imaging of the OH Near infra-Red (OHNIR) observing small-scale structures in MLT. Later, (??) identified wavelike structures, at the first time from the airglow imaging. After that, many works have been published showing gravity waves forms, using TV cameras (??). Significant step in imaging measurements was attained when (??) used Charge Coupled device (CCD) camera to observe gravity waves during the ALOHA-90 campaign. Measurements of the horizontal scale size and motion of each of these wave patterns are listed in Table 1 of (??).

In equatorial region of Brazil, the first observation of gravity waves using imaging techniques was made during the Guara campaign from August to October 1994. (??). Figure 2.4 shows four examples of the gravity waves imaged during this campaign. In Figure 2.4(a) a well-developed extensive OI(557.7 nm) band display is evident. The waves were observed for more than 5 hours as they progressed toward the northeast. Figure 2.4(b) illustrates a similar wave pattern recorded in the NIR OH emission approximately one month later. Figure 2.4(c) shows an example of a ripple display. During the Guara campaign over 25 ripple events were recorded yielding novel measurements of their velocities and observed periods. The OI (557.7 nm) image of Figure 2.4(d) shows an extensive set of N-S aligned ripples in the zenith and eastern sky superimposed on a faint band pattern that was observed to progress from low elevations toward the equator, again on an ENE heading. Since then, many gravity waves observation have been made (??) including the two consecutive SpreadFEx campaigns in 2005 and 2009 (??).

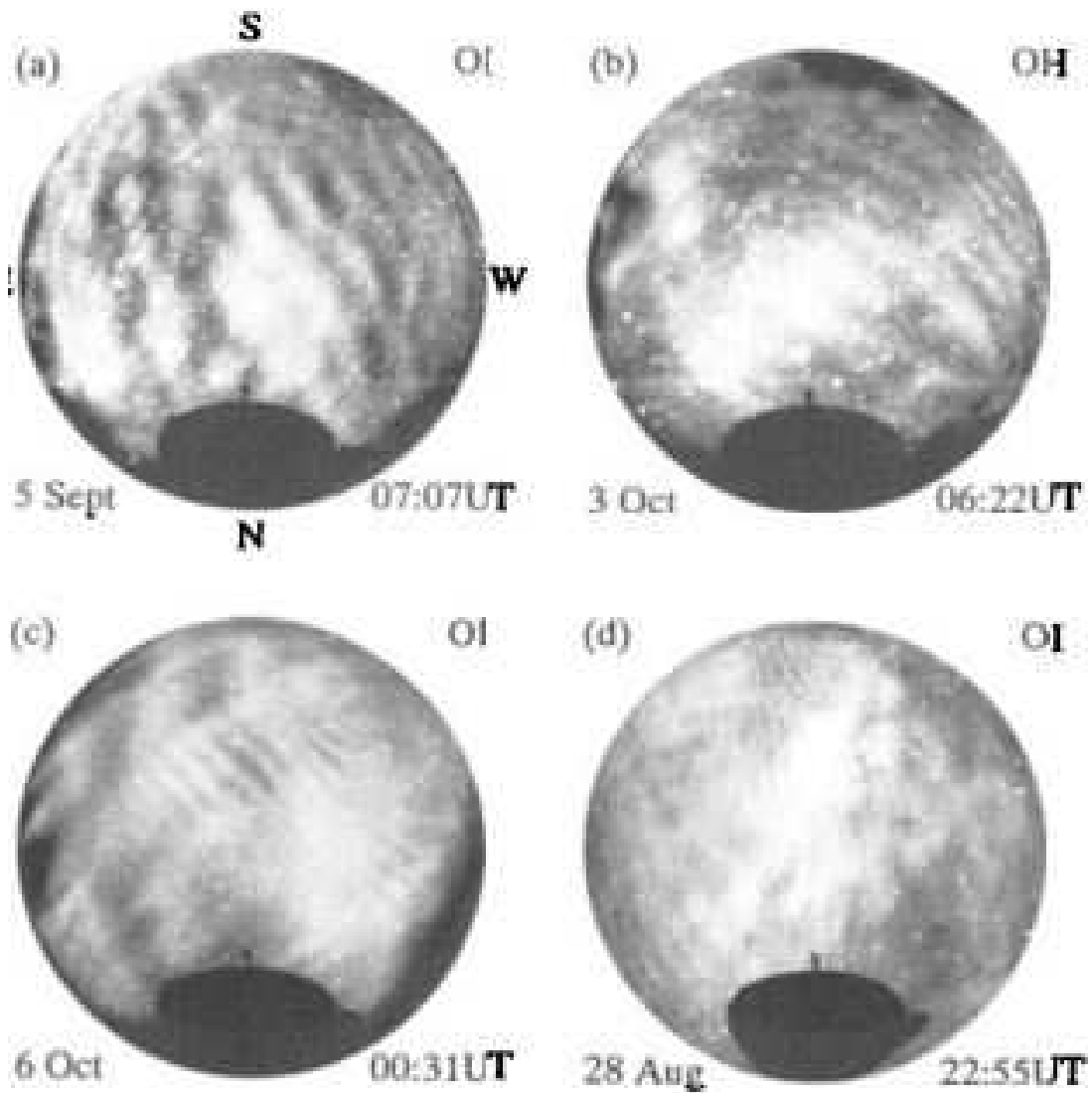


Figura 2.4 - Four images showing examples of gravity wave structure recorded in the OI(557.7 nm) and near-infrared OH emissions during the campaign:(a, b) extensive bands; (c) example of transient ripples; (d) a complex mixture of band and ripple waves. Note that the oval silhouette at the bottom of each image is the Instituto Nacional de Pesquisas Espaciais satellite tracking antenna, while the dark patches at low elevations in (b) and (c) are clouds ??)

??) compared the west-east Keograms for Cariri (a), and Brasilia (b), for the night of 1-2 October as shown in [Figura 2.5](#). In each plot, the top border corresponds to east and the lower border to west, with zenith indicated by the horizontal dashed line. On this night, airglow data were obtained for about 10 hours at each site. The Milky Way was not removed in our image processing and is visible in each plot as a bright curved band initially near the zenith, moving westward with time and exiting the cameras field of view around 01:00-02:00UT (later at Brasilia due to $\sim 12^\circ$ longitude difference between the two sites). Inspection of the Cariri data shows several coherent linear structures with a clear forward tilt. These are the signature of a medium-scale gravity wave that was most prominent from $\sim 21:00$ to 02:00UT. The forward tilt indicates the direction of the zonal wave component (which in this case was eastward), while the angle of tilt yields its zonal speed. By combining together the north-south and east-west Keogram information the parameters of the medium-scale waves are readily determined. For this event at Cariri the medium-scale wave had a horizontal wavelenght of 265 km, a phase speed 69 m/s, an observed period of 64 min and progressed on a heading of $\sim 83^\circ$. For comparison, the Keogram data from Brasilia shows strong evidence of persistent short-period gravity wave activity progressing eastwards as shown in [Figura 2.5\(b\)](#) (indicated by the forward tilted fine scale structure), modulated by a larger-scale wave progressing in the same direction.

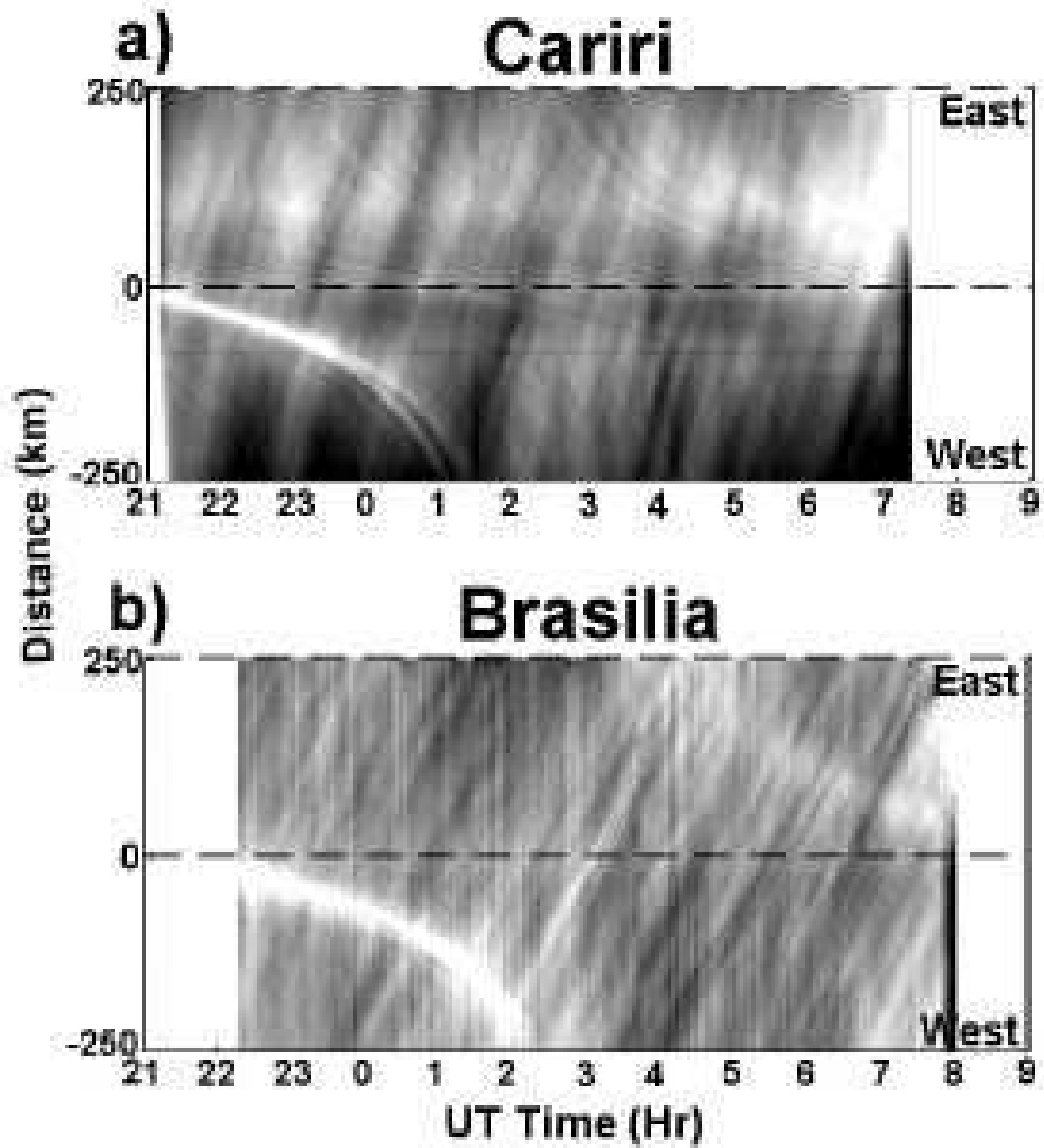


Figure 2.5 - Example west-east Keograms for (a) Cariri and (b) Brasilia obtained on the night of 1-2 October. The medium-scale gravity waves appear as coherent, tilted bands. ??)

Figure 2.6 also shows Keograms of the 6300 images in the NS (top, left) and E-W directions (top, right) as a function of time created by ??) during the spreadFex 2009. In this case, the first few depletions before 24:00UT can be seen only in the northern sky. After 00:30 UT a well developed (meridionally extended) bubble (B6) appeared over the zenith and drifted toward the east. Then, the other extended bubbles can be seen in the western sky but not reaching the zenith. The zonal drift velocity was reduced after 01:00 UT approaching the local midnight (03:00 UT). The bottom side panels of the figure are Keogram of the OHNIR images showing what was going on in the mesosphere. Several wave structures propagating from NW to SE can be seen. Between 23:30 UT and 00:30UT over zenith, a large amplitude oscillation with a period of about 1 h (GW3) can also be seen.

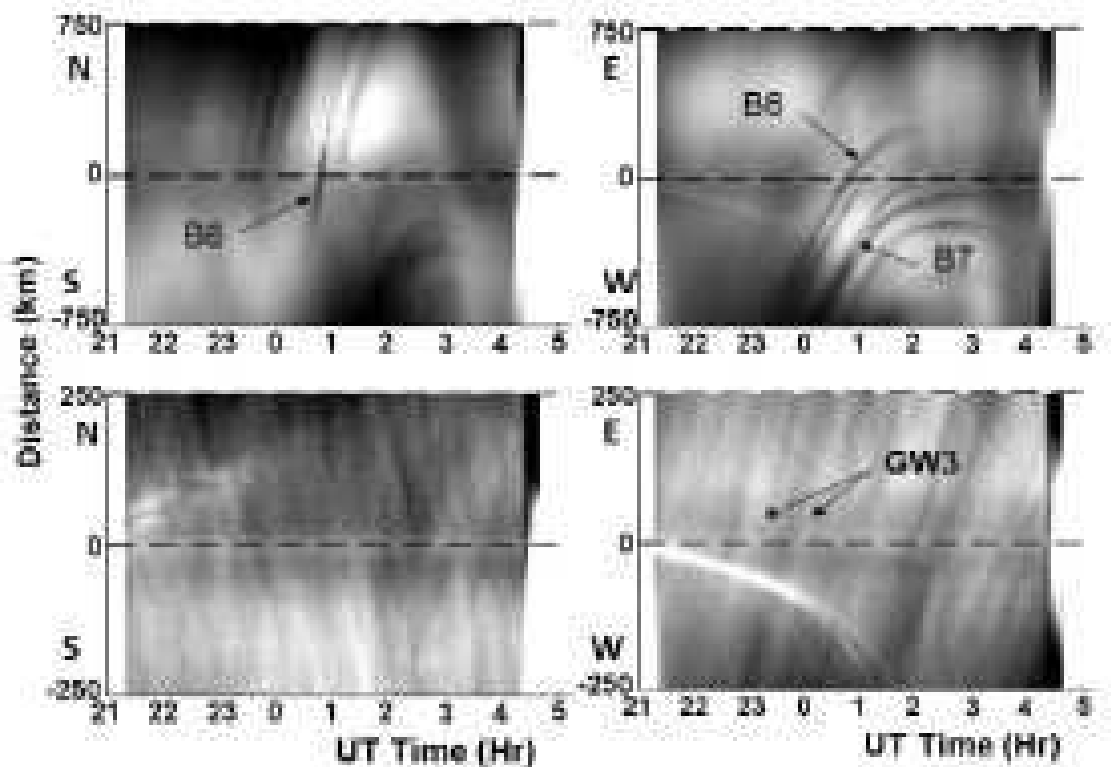


Figure 2.6 - Keogram of the flatfield images of OI 6300 (top) and OHNIR (bottom) at Cariri on 30 September 2005: N-S cut (leftside) and EW cut (rightside).

??) also used data from the mesospheric OH airglow imaging system operated at Sao Joao do Cariri ($7.0^{\circ}S, 36^{\circ}W$) from October 2000 to December 2004. Despite the limitations imposed by meteorological conditions, approximately 3540 hours of useful image data were recorded from about 500 nights, for which 1010 wave events were detected. From the total number of wave events, 48% were bands, while 52% were ripples which were all Small Scale Gravity Waves. Frequency of occurrence of the wave events (bands and ripples) for each month during the period of observation were estimated using Keogram analysis. The mean occurrence rate was 0.3 event/h . From his result, the wave activity was high in 2001 and low in 2002. However, it was not clear whether there was an interannual variation or not. In 2003 and 2004, the wave activity was low during the period of February and April.

??) also studied GWs signatures extracted from OH airglow observations using all-sky CCD imagers at four different stations: Cachoeira Paulista (CP) ($22.7^{\circ}S, 45^{\circ}W$) and Sao Joao do Cariri ($7.0^{\circ}S, 36^{\circ}W$), Brazil; Tanjungsari (TJS) ($6.9^{\circ}S, 107.9^{\circ}E$), Indonesia and Shigaraki ($34.9^{\circ}N, 136^{\circ}E$), Japan as shown in figure 2.8. The gravity wave parameters were used as an input in a reverse ray tracing model to study the gravity wave vertical propagation trajectory and to estimate the wave source region. The gravity waves observed near the equator showed a shorter period and a larger phase velocity than those waves observed at low-middle latitudes. The waves ray traced down into the troposphere showed the largest horizontal wavelength and phase speed. The ray tracing results also showed that at CP, Cariri and Shigaraki, the majority of the ray paths stopped in the mesosphere due to the condition of $m^2 < 0$, while at TJS most of the waves were traced back into the troposphere. During the summer, most of the back traced waves had their final position in the mesosphere due to $m^2 < 0$ or critical level interactions, which suggested the presence of ducting waves and/or waves generated in-situ. In the troposphere, the possible gravity wave sources were related to meteorological front activities and cloud convections at CP, while at Cariri and TJS tropical cloud convections near the equator are the most probable gravity wave sources. The tropospheric jet stream and the orography were thought to be the major responsible sources for the waves observed at Shigaraki.

Moreover, ??) studied the effect of Solar activity effects on gravity activity inferred from Low Frequency (LF) nighttime radio wave absorption in the lower ionosphere at Pruhonice ($50^{\circ}N, 15^{\circ}E$) in central Europe. It observed that digital measurements performed in summer allow absorption oscillations in the period range 10-180 mins,

which were believed to reflect gravity wave activity, to be derived. The analysis of the available information (approximately 6 years of data) allowed two conclusions to be drawn as to the effects of the solar activity on gravity wave activity: 1. there was no detectable effect of the solar 27-days (solar rotation) variation on gravity wave activity in the study area. 2. there was an indication of the existence of a remarkable (factor 1.5) positive effect of the 11-year solar cycle on gravity wave activity in the winter half of the year throughout the entire gravity wave period range studied (10-180 min). The result concerning the solar cycle effect was to some extent preliminary, attributed to the available data cover only about six years (i.e. not a complete solar cycle) and they included the disturbing effect of the Mt. Pinatubo volcanic eruption. On the other hand, the difference in the gravity wave activity, even in terms of relative amplitudes, between years of high and low solar activity was remarkable, some 20-30%. The result was obtained for winter only due to the lack of sufficient amount of summer data. The shift of the average storm tracks in the northern Atlantic probably contributed to the observed effect of solar cycle on gravity wave activity according to ??). The comparison with the results from Saskatoon in Canada (??), Saint Santin in France (??), and Christmas Island in Central Pacific (??) indicated the possibility of significant macro-regional differences in the solar cycle effect on gravity wave activity. ??)observed some possible changes in the filtering properties of the middle atmosphere with solar cycle.

2.4 Linear Theory

Atmospheric gravity waves can often be described with a simple linear theory that treats them as small departures from a stably stratified background state varying only in the vertical. The restoring force for gravity wave oscillations is the buoyancy that results from the adiabatic displacements of air parcels characteristic of these disturbances. The general gravity wave solution to the linearized forms of the fundamental conservation equations are outlined below. Furthermore, the discussion about the simpler forms of the dispersion and polarization relations that result when limited portions of the possible gravity wave spectrum are considered.

2.4.1 Equation of Motion

From ??), the fundamental fluid equations in Cartesian coordinates (x, y, z) that follow from conservation of momentum, mass, and energy are shown below

$$\frac{dv}{dt} - fv + \frac{1}{\rho} \frac{\partial p}{\partial x} = X, \quad (2.1)$$

$$\frac{dv}{dt} + fu + \frac{1}{\rho} \frac{\partial p}{\partial y} = Y, \quad (2.2)$$

$$\frac{dw}{dt} + \frac{1}{\rho} \frac{\partial p}{\partial z} + g = 0, \quad (2.3)$$

$$\frac{1}{\rho} \frac{\partial p}{\partial z} + \frac{\partial u}{\partial x} + \frac{\partial v}{\partial x} + \frac{\partial w}{\partial x} = 0, \quad (2.4)$$

$$\frac{d\theta}{dt} = Q, \quad (2.5)$$

Where $\frac{d}{dt}$ represents a total, or advective derivative; (u, v, w) is the fluid velocity vector; and the terms X, Y, and Q represent unspecified forcings that could include wave-driven forces and diffusive mixing effects accompanying wave dissipation. The remaining symbols have the usual meanings: p is pressure, ρ is density ($\rho = \rho_0 \exp[-(z - z_0)/H]$) with $\rho = \rho(z_0)$ the density at reference level z_0 and H the scale height), and $f = 2\Omega \sin\phi$ is the Coriolis parameter (where Ω is the Earth rotation rate and ϕ is latitude). These five equations plus the definition of potential temperature θ ,

$$\theta = \frac{p}{\rho R} \left(\frac{p_0}{p} \right)^k, \quad (2.6)$$

define a complete set describing inviscid fluid motion. Here $p_0 = p(z_0)$, R is the ideal gas constant, and $k = \frac{c_p}{c_v}$ is the ratio of specific heats at constant pressure and constant volume. Here θ represents the temperature a parcel of air would have if lowered adiabatically from p to p_0 (i.e., potential temperature).

The unforced forms of Equations 2.1-2.6 linearized about a horizontally uniform hydrostatic basic state with background wind $(\bar{u}, \bar{v}, 0)$ potential temperature $\bar{\theta}$, pressure \bar{p} , and density $\bar{\rho}$ varying only in z are primed quantities are

$$\frac{Du'}{Dt} + w' \frac{\partial \bar{u}}{\partial z} + fu' + \frac{\partial}{\partial x} \left(\frac{p'}{\bar{\rho}} \right) = 0, \quad (2.7)$$

$$\frac{Du'}{Dt} + w' \frac{\partial \bar{v}}{\partial z} + fv' + \frac{\partial}{\partial y} \left(\frac{p'}{\bar{\rho}} \right) = 0, \quad (2.8)$$

$$\frac{Dw'}{Dt} + \frac{\partial}{\partial x} \left(\frac{p'}{\bar{\rho}} \right) - \frac{1}{H} \left(\frac{p'}{\bar{\rho}} \right) + g \left(\frac{p'}{\bar{\rho}} \right) = 0, \quad (2.9)$$

$$\frac{D}{Dt} \left(\frac{\theta'}{\bar{\theta}} \right) + w' \left(\frac{N^2}{g} \right) = 0 \quad (2.10)$$

$$\frac{D}{Dt} \left(\frac{p'}{\bar{\rho}} \right) + \frac{\partial u'}{\partial x} + \frac{\partial v'}{\partial y} + \frac{\partial w'}{\partial z} - \frac{w'}{H} = 0, \quad (2.11)$$

$$\frac{\theta'}{\bar{\theta}} = \frac{1}{C^2} \left(\frac{p'}{\bar{\rho}} \right) - \frac{p'}{\bar{\rho}} = 0, \quad (2.12)$$

Here the derivative $\frac{D}{Dt}$ is the linearized form of the time derivative,

$$\frac{D}{Dt} = \frac{\partial}{\partial t} + u' \frac{\partial}{\partial x} + \bar{v} \frac{\partial}{\partial y}, \quad (2.13)$$

primed quantities are perturbations to the background state, and $N = \left(g \frac{\partial \ln \theta}{\partial z} \right)^{\frac{1}{2}}$ is the buoyancy frequency.

According to ??), the background shear terms in Equations 2.7 and 2.8 can be neglected by assuming that (\bar{u}, \bar{v}) and N vary only slowly over a wave cycle in the vertical. The gravity wave solutions can also assume the form

$$\left(u', v', w', \frac{\theta'}{\bar{\theta}}, \frac{p'}{\bar{\rho}}, \frac{\rho'}{\bar{\rho}} \right) = (\tilde{u}, \tilde{v}, \tilde{w}, \tilde{\theta}, \tilde{p}, \tilde{\rho}) .exp \left[i(kx + ly + mz - \omega t) + \frac{z}{2H} \right] \quad (2.14)$$

These describe a monochromatic wave perturbation with wave number components (k, l, m) and ground relative (Eulerian) frequency. Substitution this into Equations 2.7-2.12 yields a set of six algebraic equations for $(\tilde{u}, \tilde{v}, \tilde{w}, \tilde{\theta}, \tilde{p}, \tilde{\rho})$.

$$-i\hat{\omega}\tilde{u} - f\tilde{v} + ik\tilde{p} = 0 \quad (2.15)$$

$$-i\hat{\omega}\tilde{u} - f\tilde{v} + il\tilde{p} = 0 \quad (2.16)$$

$$-i\hat{\omega}\tilde{w} - \left(im - \frac{1}{2H}\right)\tilde{p} = g\tilde{\rho} \quad (2.17)$$

$$i\hat{\omega}\tilde{\theta} + \left(\frac{N^2}{g}\right)\tilde{w} = 0 \quad (2.18)$$

$$-i\hat{\omega}\tilde{\rho} + ik\tilde{u} + il\tilde{v} - \left(im - \frac{1}{2H}\right)\tilde{w} = 0 \quad (2.19)$$

$$\tilde{\theta} = \frac{\tilde{p}}{c_s^2} - \tilde{\rho} \quad (2.20)$$

Where $\hat{\omega} = \omega - k\bar{u} - l\bar{v}$ is the intrinsic frequency, which is the frequency that would be observed in a frame of reference moving with the background wind (\bar{u}, \bar{v}) . The above equations can be combined to form a single equation for the perturbation vertical velocity amplitude. Demanding the imaginary coefficients of this equation go to zero gives,

$$\frac{g}{c_s^2} = \frac{1}{H} - \frac{N^2}{g}, \quad (2.21)$$

$$\hat{\omega}^2 \left((k^2 + l^2 + m^2 + \frac{1}{4H^2}) - \frac{(\hat{\omega} - f^2)}{c_s^2} \right) = N^2 (k^2 + l^2) + f^2 \left(m^2 + \frac{1}{4H^2} \right) \quad (2.22)$$

The second equation is fourth-order $\hat{\omega}$ in and is applicable to both acoustic and gravity waves. By letting the sound speed $c_s \rightarrow \infty$ we retain the compressibility term related to the background density gradient and obtain the gravity wave dispersion relation,

$$\hat{\omega}^2 = \frac{N^2 (k^2 + l^2) + f^2 \left(m^2 + \frac{1}{4H^2} \right)}{k^2 + l^2 + m^2 + \frac{1}{4H^2}} \quad (2.23)$$

or alternatively for the vertical wave number as

$$m^2 = \frac{(k^2 + l^2) (N^2 - \hat{\omega}^2)}{(\hat{\omega}^2 - f^2)} - \frac{1}{4H^2} \quad (2.24)$$

The dispersion relation relates the wave frequency to the waves spatial characteristics (wave numbers) and to the background atmosphere properties N and (\bar{u}, \bar{v}) . The gravity wave solutions above admit waves with a broad range of properties. For vertically propagating waves, (k, l, m) are real, and the intrinsic frequency is confined to the range $N > \hat{\omega} > |f|$. All parts of this spectrum can be important to middle atmosphere dynamics. Because of this wide range of properties and because the intrinsic frequency and vertical wave number can vary strongly as a wave propagates vertically through background shear and stability gradients, models describing their propagation across a wide range of conditions may need to retain all terms in Equation 2.23 in their analysis. Simpler forms representing waves in certain limited regions of this spectral space, however, provide considerable insight and will be summarized below.

The wave group velocity describes energy transport and wave packet propagation and is written as

$$(c_{gx}, c_{gy}, c_{gz}) = \left(\frac{\partial \omega}{\partial k}, \frac{\partial \omega}{\partial l}, \frac{\partial \omega}{\partial m} \right) = (\tilde{u}, \tilde{v}, 0) + \frac{[k(N^2 - \hat{\omega}^2), l(N^2 - \hat{\omega}^2), m(N^2 - \hat{\omega}^2)]}{\hat{\omega} \left(k^2 + l^2 + m^2 + \frac{1}{4H^2} \right)} \quad (2.25)$$

The sign convention assumes that $\hat{\omega}$ is positive definite. The vector (k, l) defines the direction of horizontal propagation. Then m is negative for upward group velocity

and positive for downward group velocity. Thus, for eastward ($k > 0$) and upward ($m < 0$) energy propagation relative to the wind, intrinsic phase speeds are eastward $\hat{c}_x = \hat{\omega}/k$ and $\hat{c}_x = \hat{\omega}/m$ downward relative to the wind. It is important to note that the phase speed is not a vector quantity, although wave phase propagation has a direction given by the vector (k, l, m) .

Polarization relations relating perturbation amplitudes of the different variables to one another can also be derived from Equations 2.15-2.20. Some useful examples are

$$\tilde{u} = \left(\frac{(i\hat{\omega}k - fl)}{i\hat{\omega}l - fk} \right) \tilde{v}, \quad (2.26)$$

$$\tilde{p} = \frac{(\hat{\omega}^2 - f^2)}{(\hat{\omega}k + ifl)} \tilde{v} = \frac{(\hat{\omega}^2 - f^2)}{(\hat{\omega}k - ifl)} \tilde{v}, \quad (2.27)$$

$$\tilde{w} = \frac{\left(m - \frac{1}{2H}\right) \hat{\omega}}{N^2 - \hat{\omega}} \tilde{p} \quad (2.28)$$

and Equação 2.21.

3 Instrumentation and Methodology

This section discusses the instrumentation and image analysis for the estimation of the parameters of the medium scale gravity waves. The waves were observed in the OHNIR airglow emission from September 2000 to December 2010 by an all sky imager situated in Sao Joao do Cariri (7.40°S, 36.50°W).

3.1 The All Sky Imager

The All Sky Imager is an instrument that provides intensified monochromatic maps of auroral and airglow emission for various lines of interest. The ability of all sky imager to electronically tune the band pass wavelength of it's filters throughout the visible electromagnetic spectrum makes them an ideal candidate for hyperspectral imaging (????). This section describes the optical design and performance of the assembled instrument as candidate for low light hyperspectral imaging of aurora and airglow

Figure 3.1 shows the detailed assembled system of the all-sky imager. The design includes a section or a chamber for optical elements such as interference filters. The circular fish-eye view of the lens is converted by the first part of the lens into a narrow beam of only $\pm 7^\circ$ divergence. The effective aperture of optical elements that may be inserted into the filter chamber is 35 mm. The third part of the lens focuses the light from the filter chamber onto a circular image of 8 mm in diameter. The focal length $f = 3.5$ mm and the back focal length of the system is 17.5 mm, which is compatible with Camera lens mount systems. The camera head is air cooled down to -70°C to reduce thermo electrical noise.

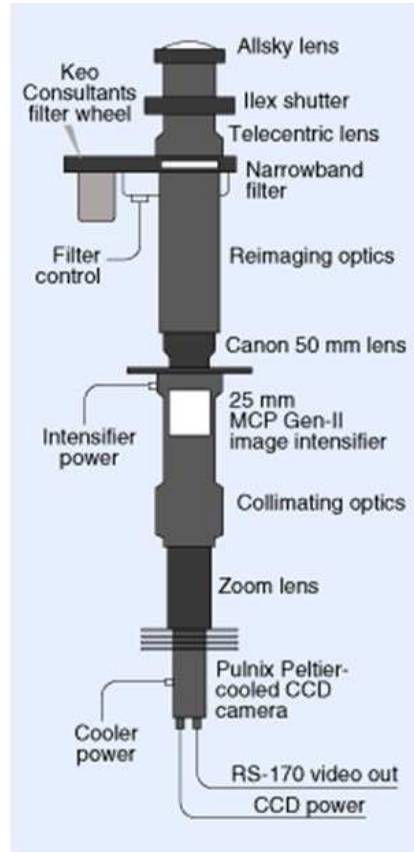
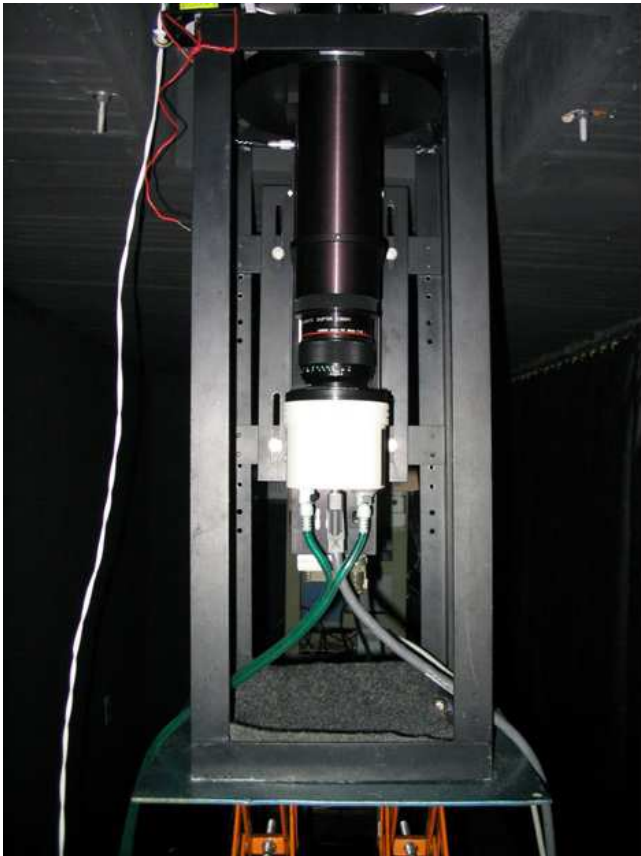


Figura 3.1 - Lens mechanics and optical diagram of all-sky lens

Airglow observations using all Sky Imaging System has been in Operation at Sao Joao do Cariri since September 2000. This imager is an optical instrument that takes high resolution images and has been designed with a fisheye lens, a CCD camera, an optical system, and an interference filter wheel. The whole system is being controlled by a microcomputer. The CCD Imager consists of a large area (6.45cm^2), high resolution 1024×1024 black-illuminated array with pixel size 14 bits. The high quantum efficiency (80% at visible wavelengths), low dark noise level (0.5 electronics/pixels/s), low readout noise (15 electrons rms), and high linearity (0.05%) makes it possible to achieve quantitative and qualitative airglow emission measurements as shown in [Figura 3.1](#). The camera uses a fast (f/4) all-sky telecentric lens system that is capable of obtaining a high signal-to-noise ratio images of 20:1, with time integration of 15s for near-infrared OH emission (715-930 nm pass band) and 90s for OI emissions (5577nm) and O_2 .

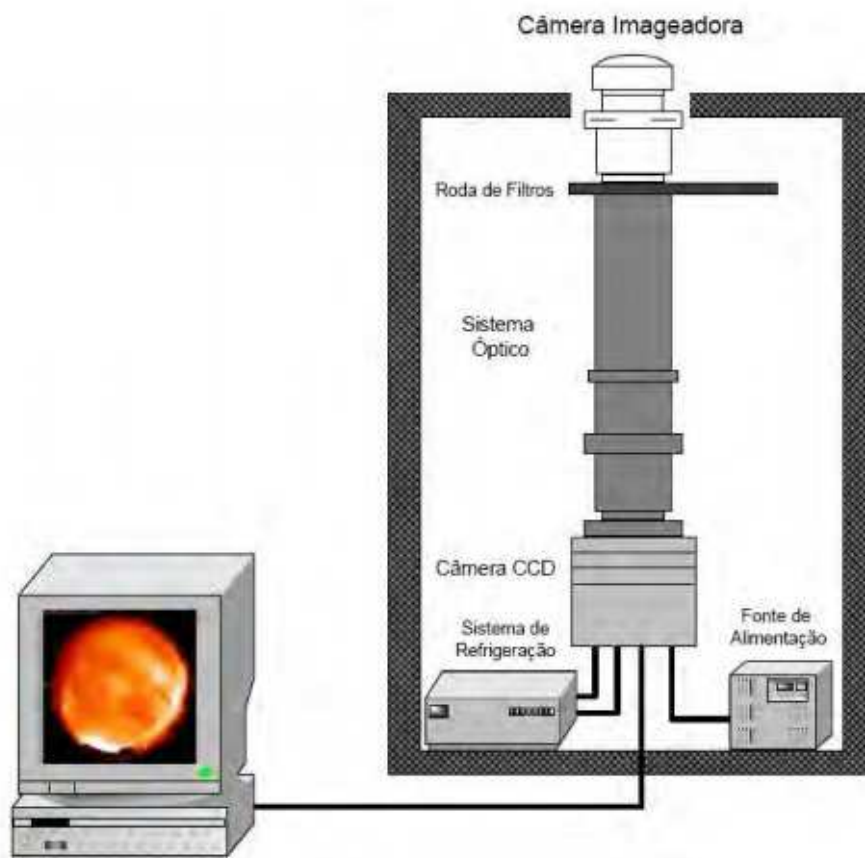


Figura 3.2 - The All Sky Imaging System: source ??)

The images were binned on chip down to a 512 X 512 resolution to enhance high signal-to-noise-ratio. For large-field information present in the all-sky data, accurate spatial calibration is essential. This can be achieved by using the stars in each image as a known reference point in the sky. The lens function is determined by performing a least-square fit using the measured position of the stars in the original image of ??).

It has been known that there are several airglow emission layers that result from chemiluminescent reactions of atomic and molecular species in the upper mesosphere. Table 3.1 lists the most prominent of these emissions in the 80-100km height range. These emissions exhibit considerable spatial and temporal fluctuations that have been attributed to the passage of atmospheric gravity waves through the airglow layers (??????).

Tabela 3.1 - Filter Information and Mean Heights for Airglow Emissions in Upper Mesosphere, Source; (??)

Filter	Filter Wavelength (nm)	Filter Band width (nm)	Mean Layer height (nm)
OI	557.7	2.67	~ 96
Na	589.2	2.37	~90
NIR OH	715-930	215	~87
O ₂ (0,1)	865.5	12.0	~94
Background	572.5	2.65	-

3.2 Period of observation and study area

The imaging system is located in São João do Cariri (7.40°S, 36.50°W) and is being operated by INPE in conjunction with Universidade Federal de Campina Grande (UFCG). Figure 3.2 shows the nominal fields of view of the all-sky imager used for the mesospheric OH gravity wave measurements (~350 km radius), assuming an emission height of ~87 km, and the thermospheric 630 nm depletion measurements (~1000 km radius) for a peak emission altitude of ~250 km. This region was chosen considered to be one of the driest places in Northeast of Brazil where the presence of clouds is very rare at night, and provide good latitudinal and longitudinal sampling of the mesospheric gravity wave field.

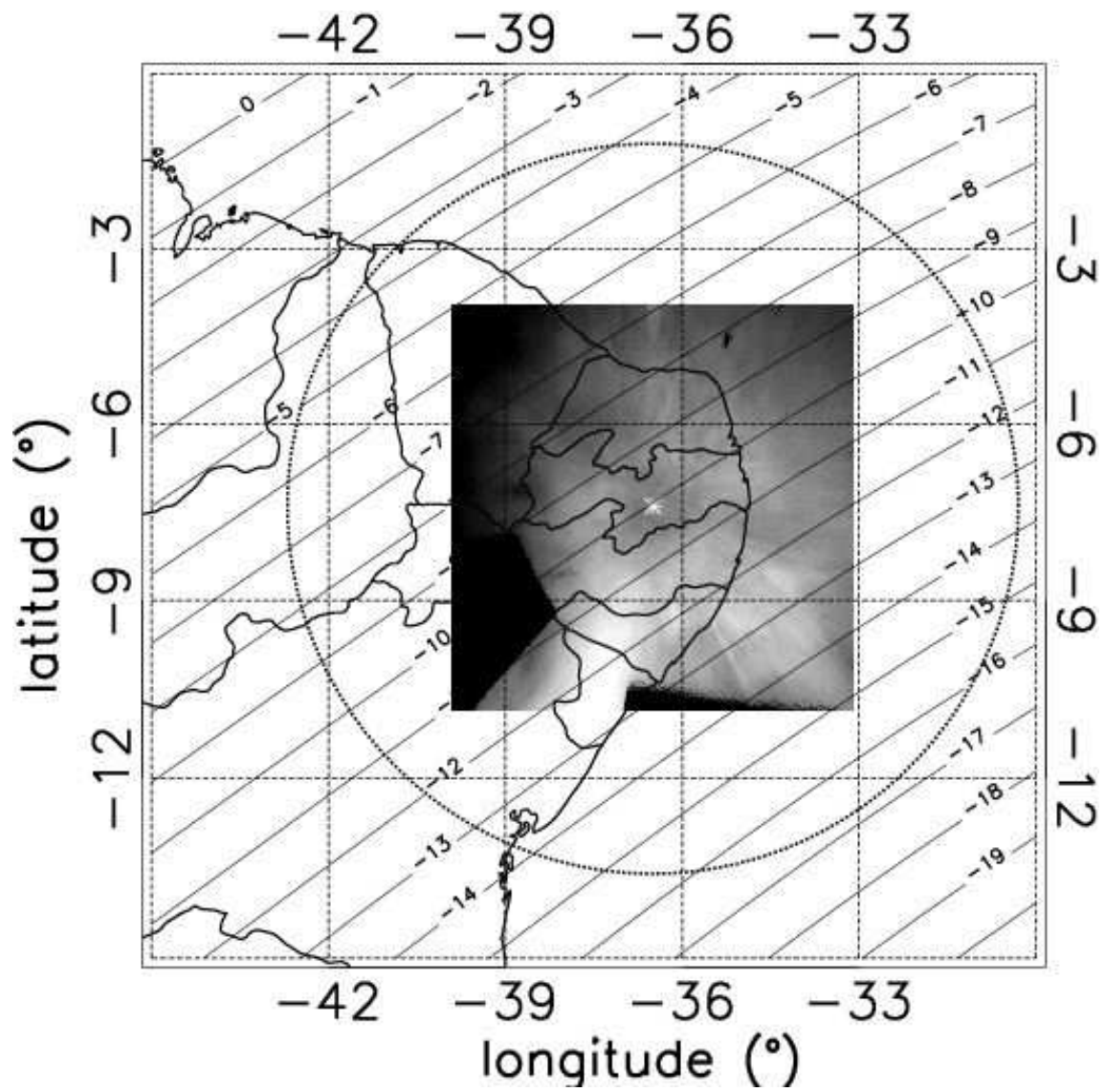


Figura 3.3 - The projection of the observation site, Sao Joao do Cariri

Long term Image measurements were made during almost 11(2000 to December 2010) consecutive years . Unfortunately,maintenance and poor weather conditions limited the measurements to at most 13 night per month during the period of observation for quantifying the mesospheric gravity wave characteristics. Figure 3.2 shows some typical images that were observed in the study site.

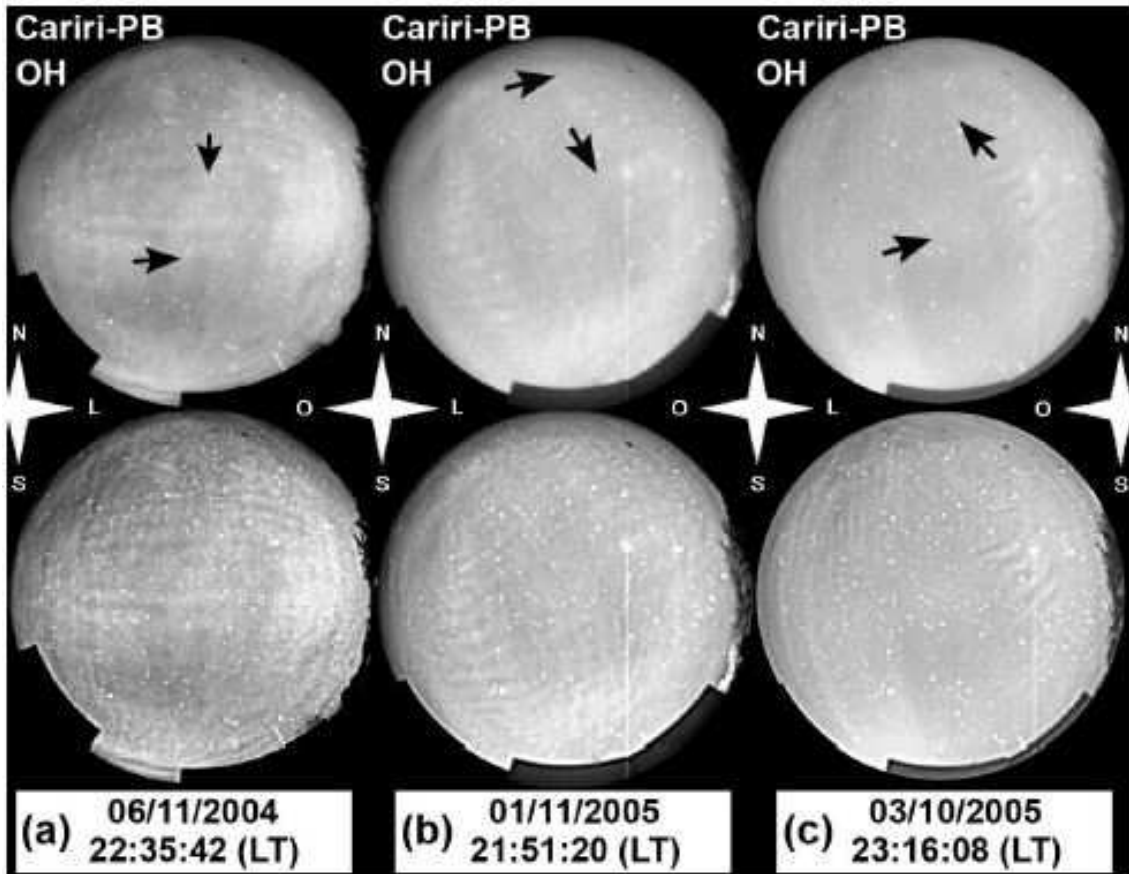


Figura 3.4 - Images observed by the all sky imager in Cariri

3.3 Determination of Gravity Wave Parameters

3.3.1 Pre-processing of the airglow images

All the images were calibrated before the analysis to determine the parameters of the MSGWs was conducted. The calibrating process can be described as a correction of the spatial coordinates of the images, i.e., the deformation caused by the fisheye

lens were minimized and the images were rotated to coincide with the geographical cardinal points. The complete pre-processing of airglow images is detailed in (??). The present pre-processing technique was also used by (????????). This can be summarized as follows:

- Rotation of the images to adjust the top with the geographical North and the center to the zenith
- Removal of the stars
- Transformation of the images into geographical coordinates system
- Contrasting adjustment to remove fluctuations due to variations of the airglow
- Filtering the images to remove unwanted spectral noise

The above procedure (does not follow any order) is shown in Figure 3.3.1 (a) Shows an image of OH observed on the night of 1st and 2nd September, 2002 in the Cariri. It can be observed that the area of the CCD (Square with Black Borders) was almost filled by the image of OH (lighter circle in the center).

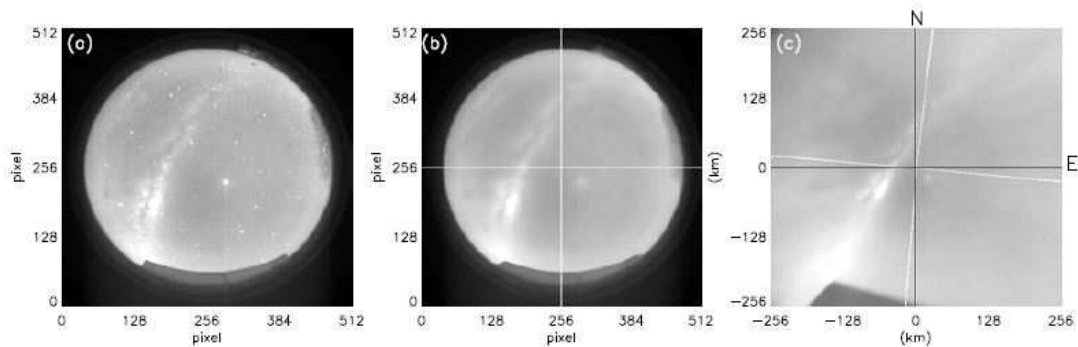


Figure 3.5 - Preprocessing of the images. (a) OH image observed from the night of 1st to 2nd September, 2002 in Sao Joao do Cariri. (b) after the stars were removed. The white lines cut through the image exactly in the center (c) linear image. Note that the white lines shown in (b) appear to be rotated and shifted to the center due to the conversion process to the geographical coordinates. The black lines indicate the true north-south direction (vertical) and east-west (horizontal).source;

Figure 3.3.1 (a) shows stars and planets observed that same night (small white spots), the tracks of the Milky Way (i. e. star cluster cutting the whole picture and turned to the northeast-southwest direction), a screen placed at the bottom of the image and branches of trees are on the right edge of the image. Figure 3.3.1 (b) is the image after the removal of the stars when the small white spots were removed almost completely. Finally Figure 3.3.1 (c) shows the linearized and rotated image to match the top with the geographical north and the right to the geographical east. The black lines illustrate the north-south and east-west directions. The white lines are the same as those shown in panel (b), so it was rotated through the linearization process. The zenith (the intersection of the horizontal and vertical lines) also slightly shifted when comparing black and white lines.

The adjustment of the zenith and correction of the effects of the edge introduced by fisheye lens were done by using a star chart for the same time and location in which Airglow image was observed. It was ensured that the stars observed in airglow image matched the actual position of the stars obtained by the star chart to the same location and time of observation. A lot of stars on the celestial chart and its corresponding position in the airglow image were found and that determined the function of the lens that mapped each pixel of the original images to a new coordinate called geographical coordinated. The algorithm for this coordinate transformation can be found in Appendix B of ??)Phd thesis. ??) described and developed software that performs all steps of the calibration of the Airglow images, making the process faster and easily executable. Conveniently, the digital image filters were applied to emphasize phenomena in a given scale. For example, to observe medium-scale gravity wave, low-pass filters with wavelengths less than 50 km were used for the removal of minor gravity waves and other small scale spectral contamination.

3.3.2 Method of Keogram Analysis

After the images were processed into keograms as described above, it was then possible to determine the horizontal parameters using the standard Keo-FFT analysis which is embedded in the Interactive Data Language (IDL), to identify and measure the monochromatic characteristics of the coherent medium-scale waves that were detectable over an extended period of time. This was done by using the white mark across the entire images (local zenith), to studied the oscillations that occurred in each direction (zonal and meridional). The parameters of the waves was obtained by geometric relations between the zonal and meridional components. Figure

3.3.2 shows twenty sequence of simulating oscillation of medium scale images. The clearest and darkest regions of the images represent the crests and trough of the waves respectively. It can be observed that the propagation direction of these waves were northwest from the observer. The horizontal white lines represent the region of interest where wave parameters were determined and this region was selected arbitrarily. The vertical axes represent the distances in meridional (top panel) and zonal (lower panel) directions and the horizontal axes indicate the time of acquisition of the images.

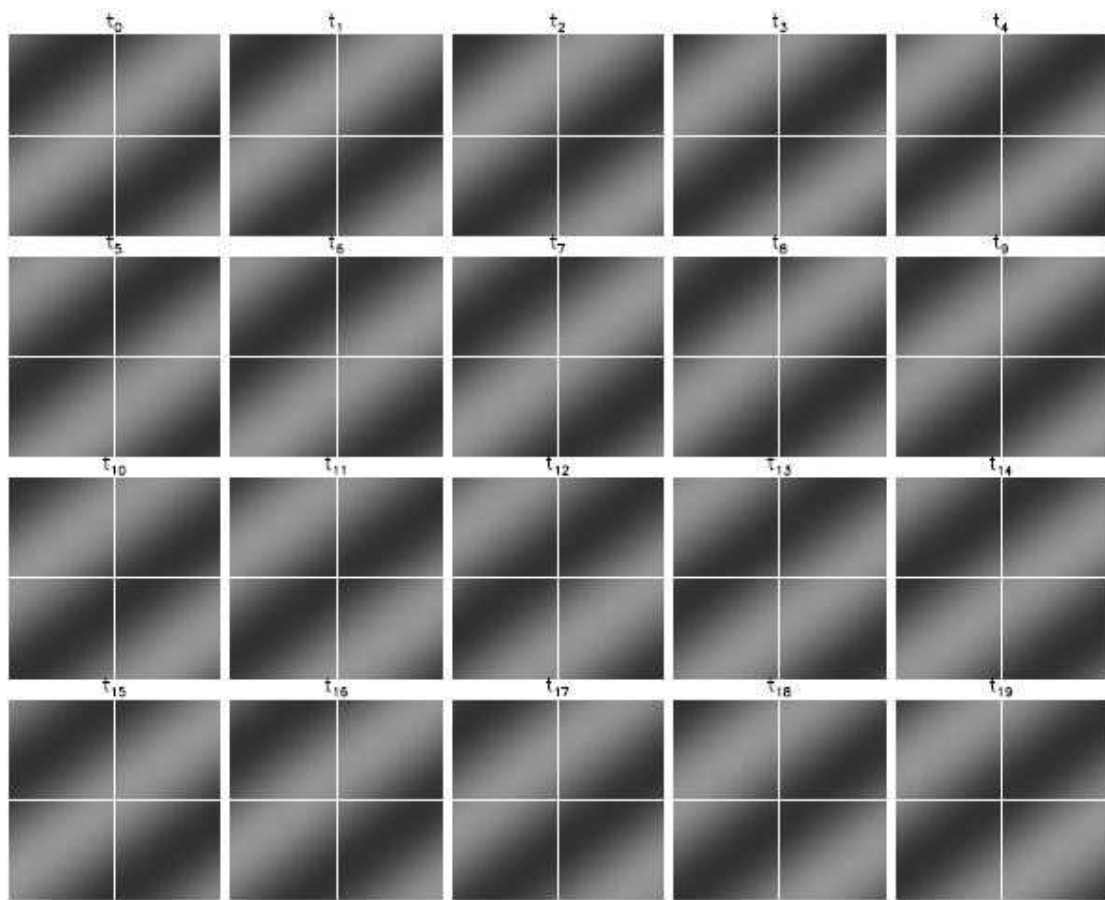


Figure 3.6 - Sequence of images showing simulated propagation of medium-scale gravity waves to the northwest. The white lines represent the regions where the zonal and meridional cuts are made for the construction of Keograms

The parameters were first obtained by visual study of the periodicity of the oscillations of a particular keogram. This was done by carefully observing the crest and trough of the sampled keogram under investigation which is illustrated in Figure 3.3.2 where the profiles of the extracted relative intensities of meridional and zonal keograms are shown by white horizontal lines. All the horizontal parameters (wavelength, period, propagation direction and phase speed) were determined by using least square method as shown in Figure 3.3.2 where a measurable squares were selected in both zonal and meridional keograms and then investigated using keo-FFT.

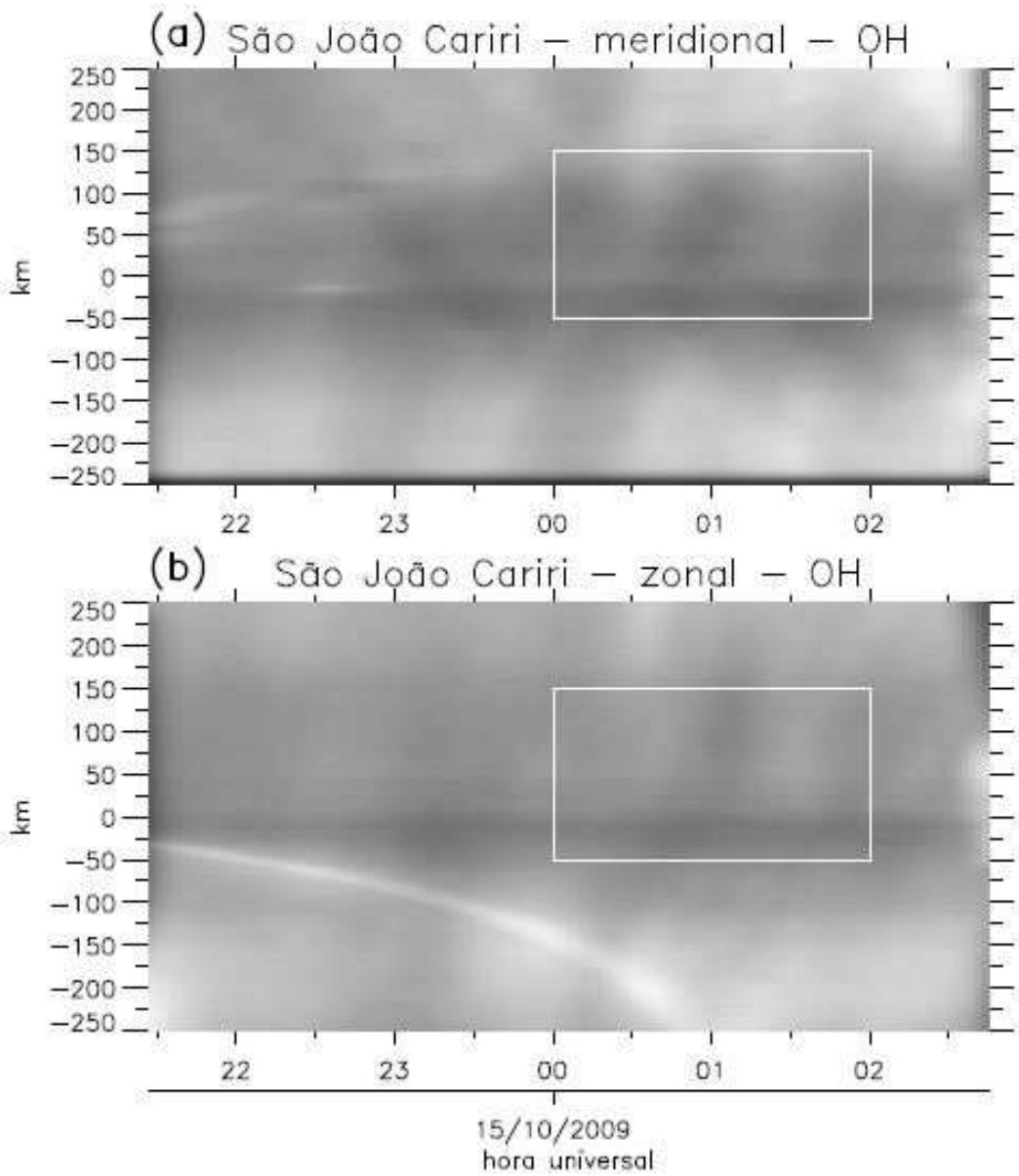


Figura 3.7 - Keogram constructed from the images of the sequence shown in Figure 3.3.2.
 (a) meridional and (b) zonal, components

This analysis automatically produced the line of best fit which indicate all the investigated parameters as shown in Figure 3.3.2. The result were done judge right if the correlation analysis is more than 0.9.

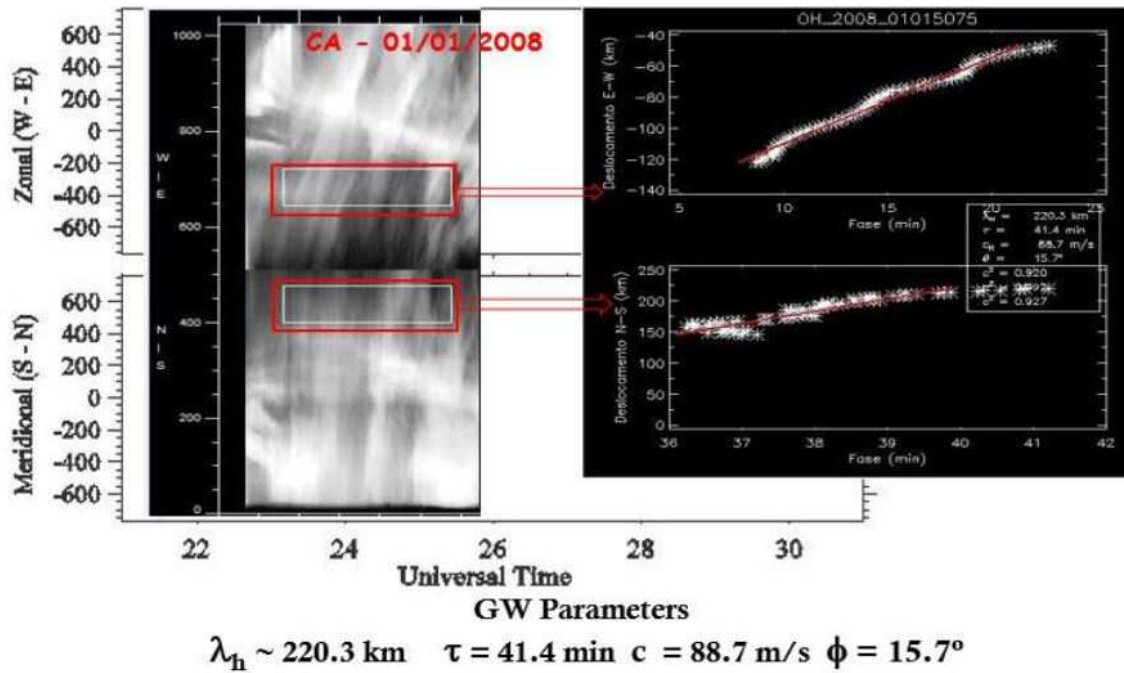


Figure 3.8 - The Line of best fit for the correlation analysis of a keogram for the estimation of the horizontal parameters

The propagation direction of the waves were verified by analyzing the slope of the line of best fit for the zonal and meridional components. Thus, it was deduced that the propagation direction was northeastward when both profile phases of zonal and meridional were increasing as shown in Figure 3.3.2 (a). On the other hand, when the two profile phases were decreasing, then it was southeast as shown in Figure 3.3.2 (b) . However, when the meridional profile phase is decreasing, and the zonal increasing, was southwest as shown in Figure 3.3.2 (c) etc.

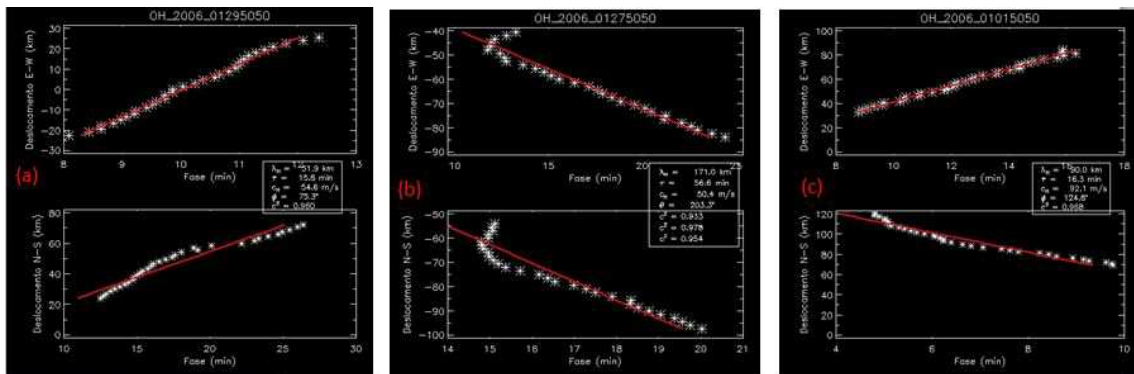


Figure 3.9 - The estimation of the phase propagation direction using the slope of the line of best fit.

The interpretation has been detailed in Table 3.3.2 showing all the possibilities of phase propagation direction when the nature of the slope of the keograms are known.

Tabela 3.2 - The approximate propagation direction of GWs obtained from the visualization of keograms. incr indicates increasing profile phase, decr 'decreasing profile phase and 'const' constant profile phase.

	N	NE	E	SE	S	SW	W	NW	Stationary
Meridional Phase	incr	incr	const	decr	decr	decr	const	incr	const
Zonal Phase	const	incr	incr	incr	const	decr	decr	decr	const

Further, verification were authenticated by animating the images that were used to create the keograms.

The horizontal wavelength follows the model below only when it is assumed that each horizontal profile selected in each keogram is a pure cosine shape of $A_i \left(\frac{2\pi t}{\tau} + \phi_i \right)$ in which τ is the period, A_i is amplitude and ϕ_i is the phase of the horizontal line i .

$$d_x = a_0 + a_1 \phi_x \quad (3.1)$$

$$d_y = b_0 + b_1 \phi_y \quad (3.2)$$

Where the indices "x" and "y" are the zonal and meridional components, respectively, "0" is linear coefficients and "1" is the angular coefficients of each straight line. The angular coefficients a_1 and b_1 are the zonal and meridional phase respectively.

$$\lambda_x = v_x \tau \quad (3.3)$$

$$\lambda_y = v_y \tau \quad (3.4)$$

The horizontal wavelength λ_H and the the phase propagation direction can be obtained geometrically as

$$\lambda_H = \frac{\lambda_x \lambda_y}{\sqrt{\lambda_x^2 + \lambda_y^2}} \quad (3.5)$$

$$\alpha = \arccos\left(\frac{\lambda_H}{\lambda_y}\right) \quad (3.6)$$

In summery, Figure 3.3.2 show the projection of the regions of interest for the keogram created from the image observed on 6th November, 2014. The right hand side shows the computed squared magnitude of the 2-D FFT. Owing to the symmetry of the 2-D FFT of real data, two mirror-image peaks in the power spectrum are evident at $(\pm 0.021 km^{-1}, \pm 0.012 km^{-1})$, corresponding to the large-scale quasi-monochromatic wave structure present. The horizontal wavelength of these waves were determined by computing the inverse of the distance of the peak from the origin, and it was found to be $47 km \pm 3$. The direction of propagation of the wave is given (with a 180^0 ambiguity, again owing to the symmetry of the keo-FFT) by the position of the peak in this k-space diagram (in this case the wave motion was progressing on a heading of either -215^0 or 55^0).

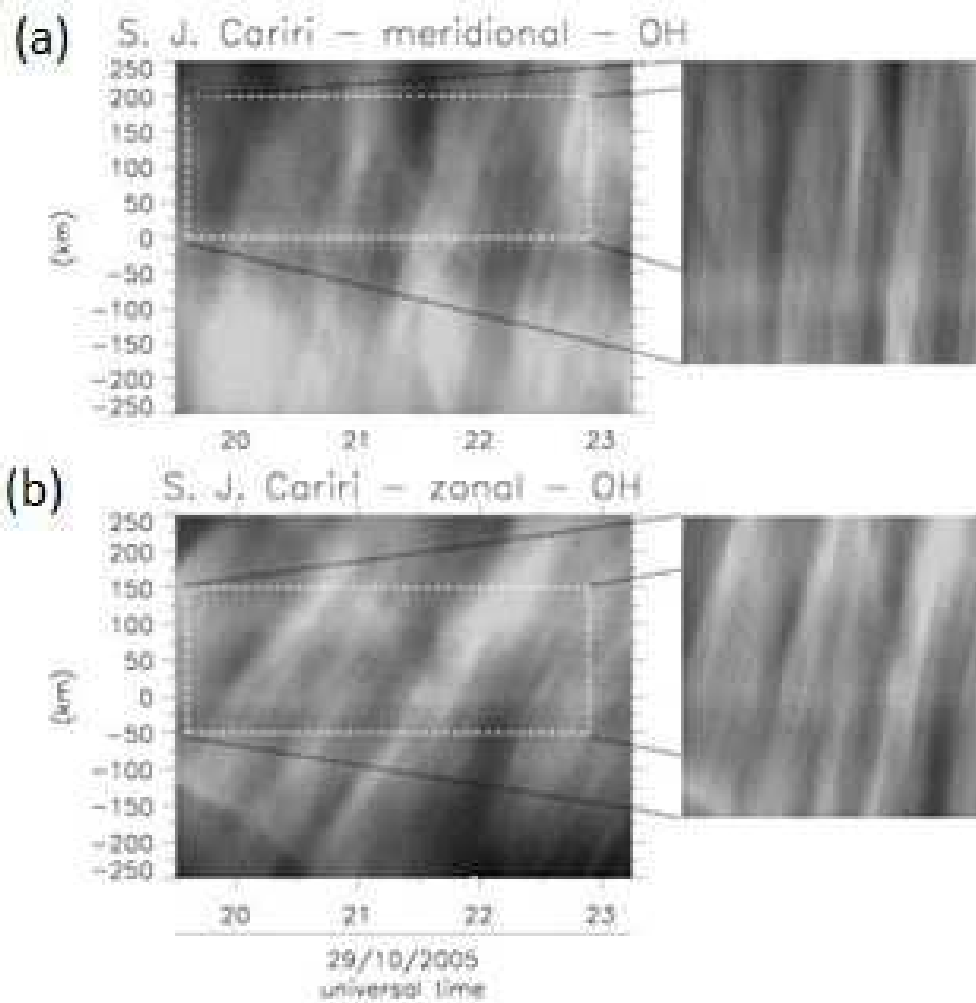


Figure 3.10 - The projection of OH NIR airglow image area

4 Results and Discussion

Measurements were taken from September 2000 to December 2010. A total of 1101 keograms were analysed, in which 573 were associated with medium-scale gravity waves which represent 424 hours period of propagation. However, about 207 number of images were found to be covered by clouds and were not useful for gravity waves analysis. These data provides essential information on the scale sizes, occurrences, directionality, seasonality and solar cycle influence of MSGWs during the occurrence of 11 years observation and analysis.

4.1 Parameters of Medium Scale Gravity Waves

4.1.1 The horizontal; Wavelength, period and phase speed

Figure 4.1.1 (a) shows the resulting distribution of the observed wave periods binned with 20 min intervals. The distribution of the periods of the MSGWs shows a clear tendency toward longer wave periods with about 85% of MSGWs exhibiting periods between 0 to 60 minutes in which the maximum being concentrated between 20 to 40 minutes. The mean wave period is 47.3 minutes and the corresponding standard deviation of 36.1 minutes. Figure 4.1.1 (b) shows the distribution of horizontal wavelength of MSGWs as a function of the number of events. The data were binned into histograms of 50 km width. The band distribution exhibited a significantly broader range of horizontal wavelengths extending from 50 to 500 km, in which 90% of all MSGWs exhibited range of 50 to 300 km with maximum occurrence being concentrated between 100 to 150 km. The mean wavelength is 199.5 km with a corresponding standard deviation of 119.5 km as shown at the top right corner of the histogram. Figure 4.1.1(c) shows the distribution of the phase speeds of MSGWs plotted at the interval of 20 m/s. The MSGWs measurements range from 20 to 150 m/s with the maximum being concentrated between 60 to 80 m/s and exhibit a mean phase speed of 81.9 m/s and the related standard deviation of 43.6 m/s.

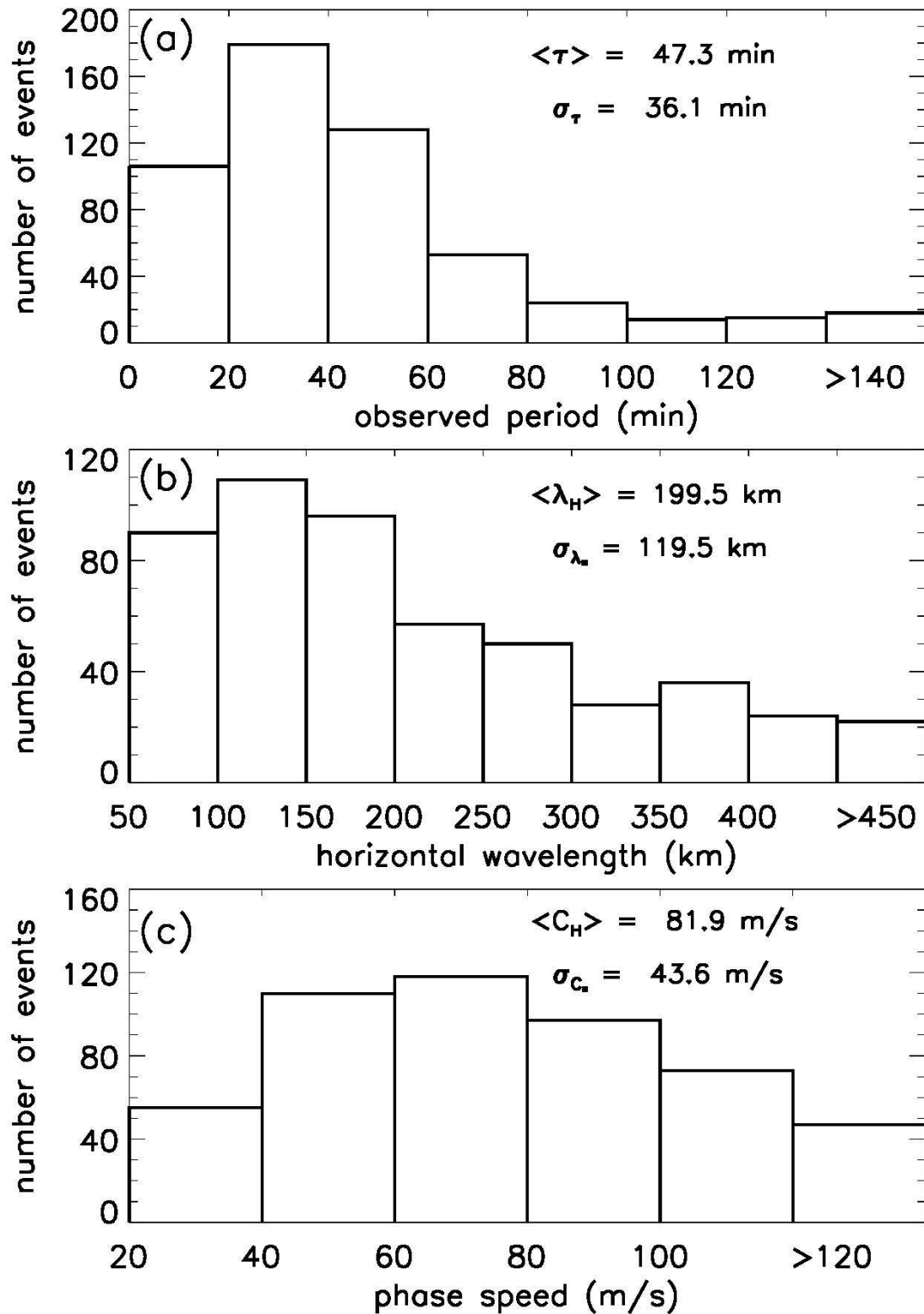


Figura 4.1 - The histogram distribution of the (a) observed periods of propagation (b) horizontal wavelengths of (c) phase speed; of the MSGWs that were observed in Sao Joa do Cariri from the year 2000 to 2010

The characteristics of the MSGWs agree very well with previous gravity waves studied by (????) from north-eastern Brazil using the same instrumentation. However, this paper studies almost 11 years observation of the medium-scale gravity waves which constitutes very important new dataset on the mesospheric properties at equatorial latitudes. These medium scale gravity waves are usually observed as ionospheric electron density perturbations termed Traveling Ionospheric Disturbances (TID's). Their characteristics have been studied extensively using ionosonde and radar techniques, reviewed by (??). Whereas Large-scale TIDs are often associated with high-latitude magnetic disturbances and can propagate large distances from their auroral source region according (??), medium scale TIDs exhibiting periods of several tens of minutes, are prevalent at mid- and low latitudes and are thought to play a major role in the development of Spread-F e.g. by (??).

The MSGW parameters obtained from the OHNIR airglow during the SpreadFex Campaign (??) showed a similar results compared to this present research results. However, a few differences have been found in these results, that the horizontal wavelength have wide range from 50 to 400 km. These resulted in relatively observed wave periods clustered around 20-60 min (typical range from 0-80 min). In any case this data was found to have somewhat larger mean and standard deviation values as shown on the right corner of the histogram distribution in Figure 4.1.1. Nevertheless, the wave events derived from the Keogram analysis are consistence with those expected from medium-scale gravity waves, and they significantly extend the usual range of gravity wave measurements by imagers. Comparison of the observed phase speeds, this work again shows a broader range with datasets exhibiting a strong preference for values around 20 to 120 m/s with a range of typically 40-100 m/s. On the other hand, these results present more years of observation analysis, but that is not sufficient to attest that the spectrum of MSGWs has a significant difference between the present results and that of the SpreadFEx campaigns.

According to (??), GW may contribute to bubble formation if it satisfies, at least, three conditions; the wave should penetrate directly to the bottom side of the F-region prior to plasma bubble formation, the wave amplitude should be larger enough to modify the thermodynamics of the local atmosphere and the wave phase speed should be sufficient to enable a resonance condition for the coupling of the wave to the plasma process (??). However, the OH-NIR waves normally desipated at an altitude (170 - 180km) lower than the F-region due to the reduction of amplitude or

if the waves encounter a critical layer. This suggests that these MSGWs events may not be able to contribute to bubble formation as a result of MSGWs dissipation and annihilation.

Moreover (??) also forward ray traced the medium-scale GWs from the OH layer into the thermosphere and found that 2 of the waves, the GWs with $\lambda_H=61.4$ and 148.3 km, did not penetrate very far above the turbopause at $z\sim 110$ km. This was not surprising, because these GWs had slow horizontal phase speeds of $C_H < 30\text{ms}^{-1}$. Although very sensitive to the chosen wind model, they found that the GWs with $\lambda_H=145.1$ km and 64 km likely did not penetrate above $z\approx 165$ km. However, they also found that two of the GWs with $\lambda_H=71.4$ km and 158.6 km, may have penetrated to $z\geq 170$ km, which is high enough to potentially seed equatorial spread F (ESF) or plasma bubbles at $\sim 10^\circ$ from the magnetic equator, where the field lines are lower than at the magnetic equator. Since these waves would have reached $z\sim 170$ km only $3-6^\circ$ south of the magnetic equator, they may not have reached a high enough altitude at that magnetic latitude to seed ESF, however, most of the medium-scale gravity waves events in this paper have $C_H > 60\text{ms}^{-1}$, which implies that several of them can propagate to the bottom side of F region of the ionosphere to seed ESF. Also medium-scale GWs identified by (??) forward ray traced to near the bottomside of the F layer, using a wind model and meteor radar winds at Cariri. (??) found that the horizontal scale of the measured GWs in the OH layer compared well with the inter plasma-bubble distances in the ionosphere, suggesting a direct link between these GWs and the seeding of plasma bubbles.

Furthermore, the gravity wave propagating model reported by (??) and (??) is useful to understand the importance of fast MSGWs when they are propagating upwards in the thermosphere-Ionosphere (TI) region. The model used an inelastic relation of dispersion which is derived from the compressible fluid equations with molecular viscosity and thermal diffusivity. The evolution in space and time of gravity wave packet was computed using a ray tracing methodology (??). Some horizontal and vertical propagation and dissipation characteristics were calculated and discussed by (??). Also, most of the MSGWs, with horizontal wavelength (λ_H) shorter than 200 km and vertical wavelength (λ_z) shorter than 20 km, can attain the altitudes below 150 km prior to start dissipation. This really implies that the MSGWs, discussed in the present work can propagate to the said altitude. Consequently the events of the horizontal wavelength and phase speed that are between the range of 100 to 450 km

and faster than 60 m/s respectively are in more favorable condition of penetration into the TI before they dissipate. In this case, the altitudes prior to dissipation is the altitude where the gravity wave momentum flux is maximum and this altitude, the gravity wave will lose its momentum and energy dissipating, eg ??).

4.1.2 Phase Propagation direction and Seasonality of Medium Scale Gravity Waves

The phase propagation direction was binned over 90^0 intervals are plotted in [Subseção 4.1.2](#) (total). The total distribution of MSGWs is highly anisotropic, exhibiting two directions of preference; southeast (azimuth range 90^0 - 180^0) and northeast (azimuth range 0^0 - 90^0) with the later being dorminant.

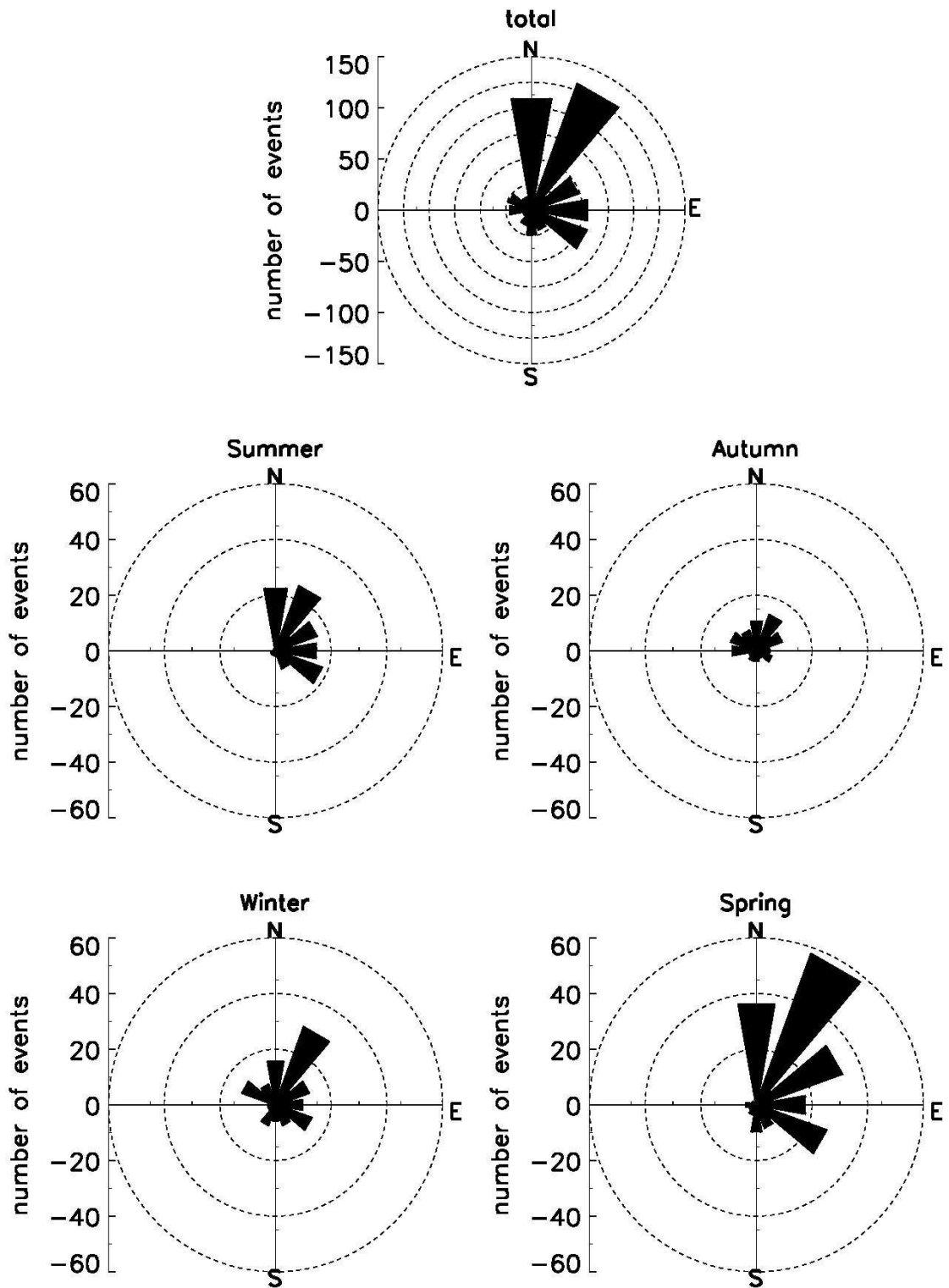


Figura 4.2 - The seasonality of the propagation direction of the MSGWs

In order to examine the seasonal tendencies of the medium-scale wave parameters, the data has been represented in four seasons which are; summer (January, February and March), autumn (April, May and June), winter (July, August and September), and spring (October, November, December) as shown in [Subseção 4.1.2](#). The MSGWs showed a clear seasonal variation for phase propagation direction. It can be observed that the summer and winter show Northeast preference in the directionality of the wave events. In summer and spring the preferential propagation direction is toward northeast while in winter and autumn, no preferential propagation direction is observed (they are evenly distributed).

The MSGWs was further investigated to know how the number of MSGWs events changed from one month to another or season to season. [Figura 4.1.2](#) shows a histogram distribution of seasonal variation for the number of waves events that were observed during the almost 11 year period of observation. The maximum occurrences are seen in October, November and September which are within spring and the end of the within season respectively. The minimum number of events are seen in April and May which are within Autumn season. The percentages on top of each bar show the cloudless wave events that were observed within the corresponding month. Moreover, most of the MSGWs events propagate preferentially to northeast (NE) and a few to northwest (NW).

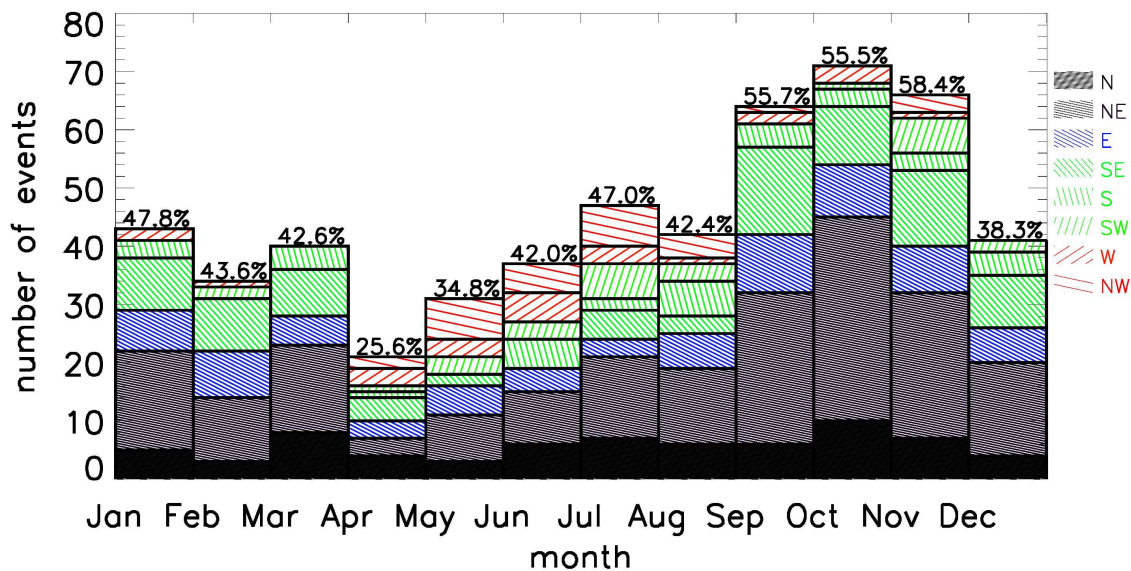


Figura 4.3 - The total number of MSGWs observed as a function of the Months (The colors represent the propagation direction)

The month-to-month variability is probably due to the primarily variability of meteorological (tropospheric) sources of gravity waves. The anisotropy of the wave propagation direction observed during the four seasons, mainly in summer and winter could be due to seasonal variation of the stratospheric and mesospheric wind fields. Also the observations of OH airglow images obtained in the winter and spring season (September, October, and November) indicate a tendency for long period gravity waves (>1 hour) to propagate in the northeastward direction. This suggested that this preferential direction of the gravity waves could be a result of blocking at a critical layer produced by the interaction of the upward propagating waves with the horizontal background flow.

Moreover (??) concluded that convection was not a prominent source for the wave events observed well to the east at Cariri. Meanwhile, (??) suggested that, about 24% of the observed gravity waves originated in the troposphere and identified that the wave source regions were placed in the west and northwest side of the observatory at Cariri, where deep tropospheric convection frequently occurs. Thus the anisotropy in this study can be attributed to the sources region of the MSGWs events.

(????????) have stated that the gravity waves observed at the site exhibited the almost the same azimuthal distributions irrespective of the wave scales. The medium-scale waves all progressed eastwards but with a strong preference for Northeast motion. A similar results were obtained by (????) using OH airglow measurements during the Guara and spreadFex campaigns. (??) also achieved the same result when studied small-scale gravity waves, which suggest that the observed eastward distribution is a regionally and seasonally recurrent phenomenon.

The anisotropy can be attributed to be the changing gravity wave source region for the observer. This is normally significant at mid latitudes where the zonal wind system is strong (higher than ± 40 m/s) according to (??). Meanwhile, (??) made it emphatically that in the equatorial region, the zonal winds are weak, less than ± 20 m/s, except in summer (± 40 m/s). Therefore, the source region with respect to the observer is an important factor with respect to the propagation direction seen at Sao Joao do Cariri. Thus, the MSGWs sources can be from the South American continent (??). Moreover, the possible sources and causes of MSGWs are related to meteorological front activities and tropical cloud convections near the equator as reported in (??).

The anisotropy detected in propagation direction of the MSGWs, mainly for the 4 seasons could also be due to the presence of a critical level, (??). Gravity waves propagating upward from the lower atmosphere are absorbed into the mean flow as they approach a critical layer where the intrinsic frequency of the wave is doppler shifted to zero. This situation can at any height when the local horizontal wind speed along the direction of propagation is equals to the observed horizontal phase speed of the gravity wave. The theory of gravity wave absorption at critical layers is well developed by ??????????????????). At the height of the critical layer a horizontal surface can be constructed to give a polar plot called blocking diagram showing the range of azimuthal angles and speeds of gravity waves forbidden from further upward propagation ??????????). Gravity waves with horizontal phase velocity and directions within this region would encounter heavy absorption as they approach to the critical layer. Gravity waves with horizontal phase velocities outside this region would not meet by chance a critical layer and should be observable. The Doppler-shifted frequency, Ω , due to the horizontal wind V_0 is given by

$$\Omega = \omega - k_x V_{0x} \quad (4.1)$$

where ω is the source frequency, k_x , is the magnitude of the horizontal wave vector, and V_{0x} is component of V_0 along the wave propagation direction. Equation 4.3 can be rewritten as

$$\Omega = \omega \left(1 - \frac{V_{0x}}{v_x} \right) \quad (4.2)$$

where v_x is the observed horizontal phase speed of the wave. Equation 4.2 can be expressed in terms of the zonal and meridional wind components (V_z, V_m) as

$$\Omega = \omega \left(1 - \frac{V_z \cos\theta + V_m \sin\theta}{v_x} \right) \quad (4.3)$$

Therefore, at the critical layer when V_{0x} tends to v_x and Ω tends to zero, the Equation 4.4 can be written as

$$v_x = V_z \cos\theta + V_m \sin\theta \quad (4.4)$$

Equation 4.4 can be represented in a polar plot of v_x for every azimuth knowing (V_z, V_m) . This blocking diagram is used to find regions with $\Omega \leq 0$ or the forbidden regions at any height below the peak of the emission layer for each propagation direction ϕ and phase speed v_x .

In other to explain how the critical layer affect the propagation of the gravity waves, the above model have been used to plot a 'blocking diagrams' for each season using the wind profiles from HWM-93 and 2003 MSGWs data observed. The wind model shows a clear seasonal variation from in all the four seasons summer, autumn, winter and spring. Figure 4.1.2 shows a 3-D blocking diagram from 0 to 96 km.

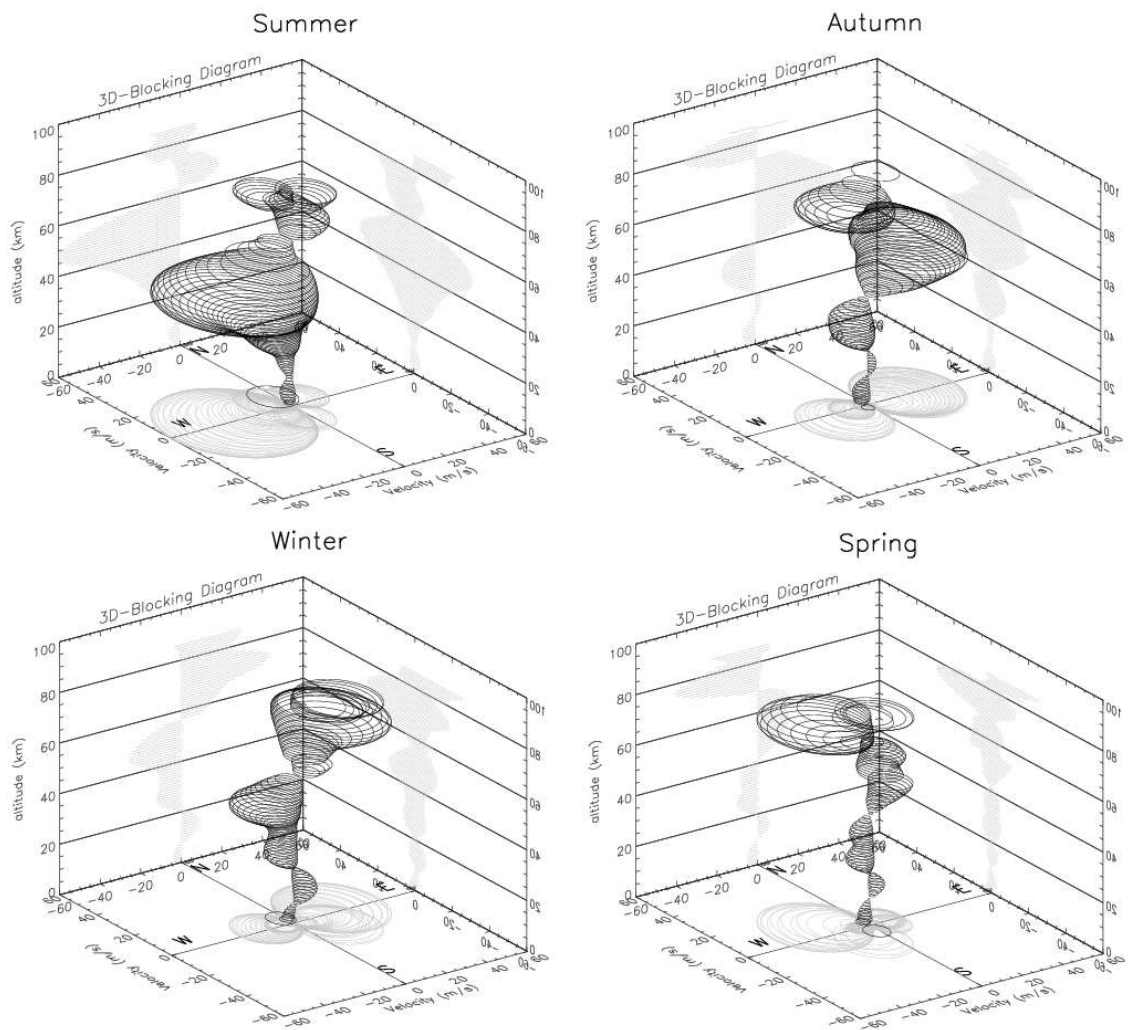


Figure 4.4 - Three-dimensional blocking diagram from 0 to 98Kkm for the 4 seasons in the year 2003

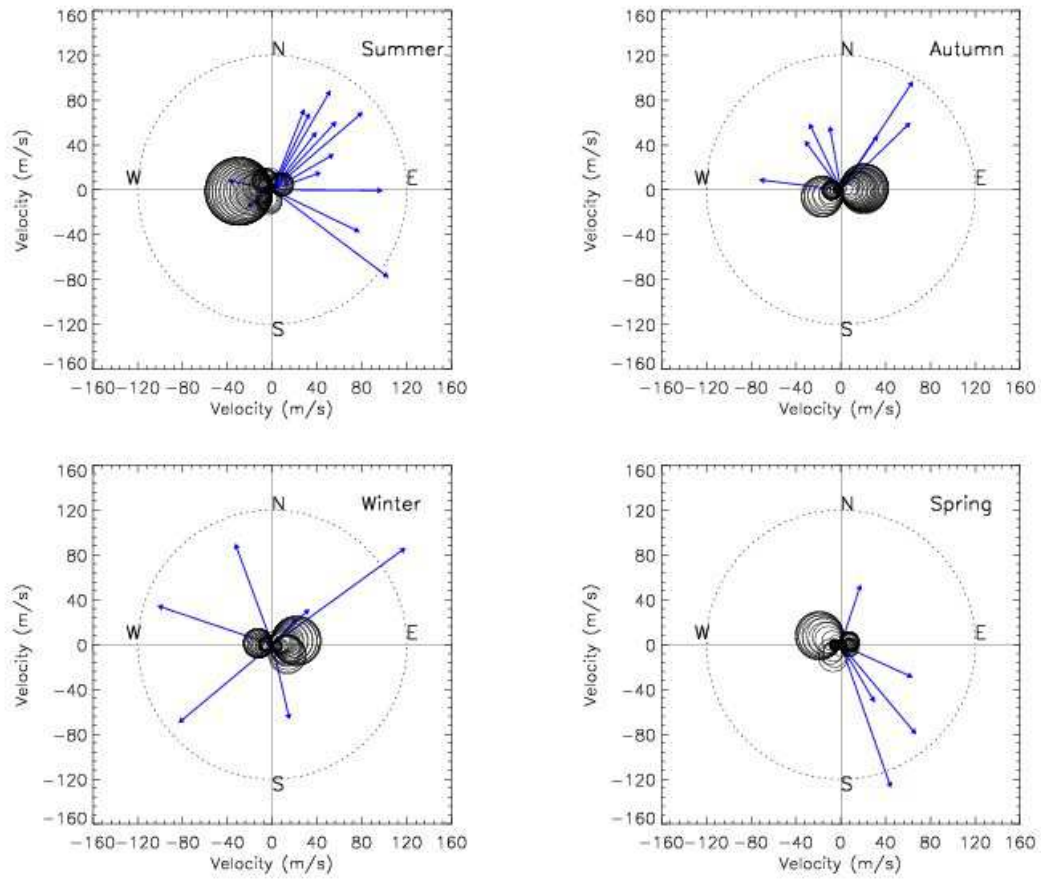


Figure 4.5 - Blocking diagram the four seasons showing the OH layer at height 86 km. The arrows indicate the magnitudes and directions of the phase velocity of the waves during each season

Figura 4.1.2 shows the top view of Equação 4.1.2 for each season and these superimposed with the waves observed for each season in the year 2003 for the OH NIR airglow emissions. In general, some of the waves were out of the forbidden region and according to ??) those waves in the forbidden region may be ducted waves that propagated from a large horizontal distance or doppler shifted outside the forbidden region ??). It is expected that the critical layer may allow the waves to survive within the layer and penetrate into the higher altitudes. However, in winter, autumn and spring most of the waves were trapped in the forbidden region and did not survive which makes them unmeasurable or unobservable. Moreover, in winter the MSGWs encountered a lot of critical layers and a few wave events were able to propagate further. Mean while summer seems to be very different from the other seasons since the critical layer was located opposite to the phase propagation direction of the MSGWs. Moreover, the waves that survive the critical layer also prove that MSGWs are less susceptible to wind filtering effects than that many of the smaller-scale waves, due to their larger scale sizes and somewhat higher phase speeds (typically 40-80 m/s), and are therefore better suited for ray tracing studies to identify potential source regions ??). As a result, the influence of the wind filtering alone can not be used to justify the directionality of the phase propagation direction of MSGWs events.

The images measured and the model predictions are almost in accordance with the prediction of the forbidden regions and the observed phase propagation direction of the MSGWs. The anisotropy of the observed waves could be attributed to non-uniform sources of the gravity. ??) suggested that the wind in the middle atmosphere can be large compare with the apparent phase velocity of the waves, therefore, it is most likely that the anisotropy in the data resulted from directional filtering of an ensemble of wave motions. However, more measurements are needed from other observational instruments before any conclusion can be drawn on the anisotropy of the phase propagation direction. Nevertheless, this results agree with the anisotropy detected in the propagation direction of the MSGWs which affirms that wave filtering by winds can play an important role in the seasonal variation of the waves over the equatorial.

4.1.3 The parameters of MSGWs and solar cycle

This section will study the evolution of the MSGWs according to the solar cycle. In order to address, the question of how variations of solar activity influence the MSGWs events in the MLT or not, the evolution of the 11 years dataset were inves-

tigated by using solar flux F10.7 parameter. The histogram in Figure 4.1.3 shows the number of events of the MSGWs that were observed from 2000 to 2010 and the F10.7cm solar flux (right hand axis). The maximum occurrence of the MSGWs propagation was in 2004 and the minimum was concentrated in 2000 and 2010. The MSGWs events increased from 2000 to 2004 and decreased from 2004 to 2010. The percentage of the cloudless wave events within each year has been indicated on top of the bars of the corresponding year.

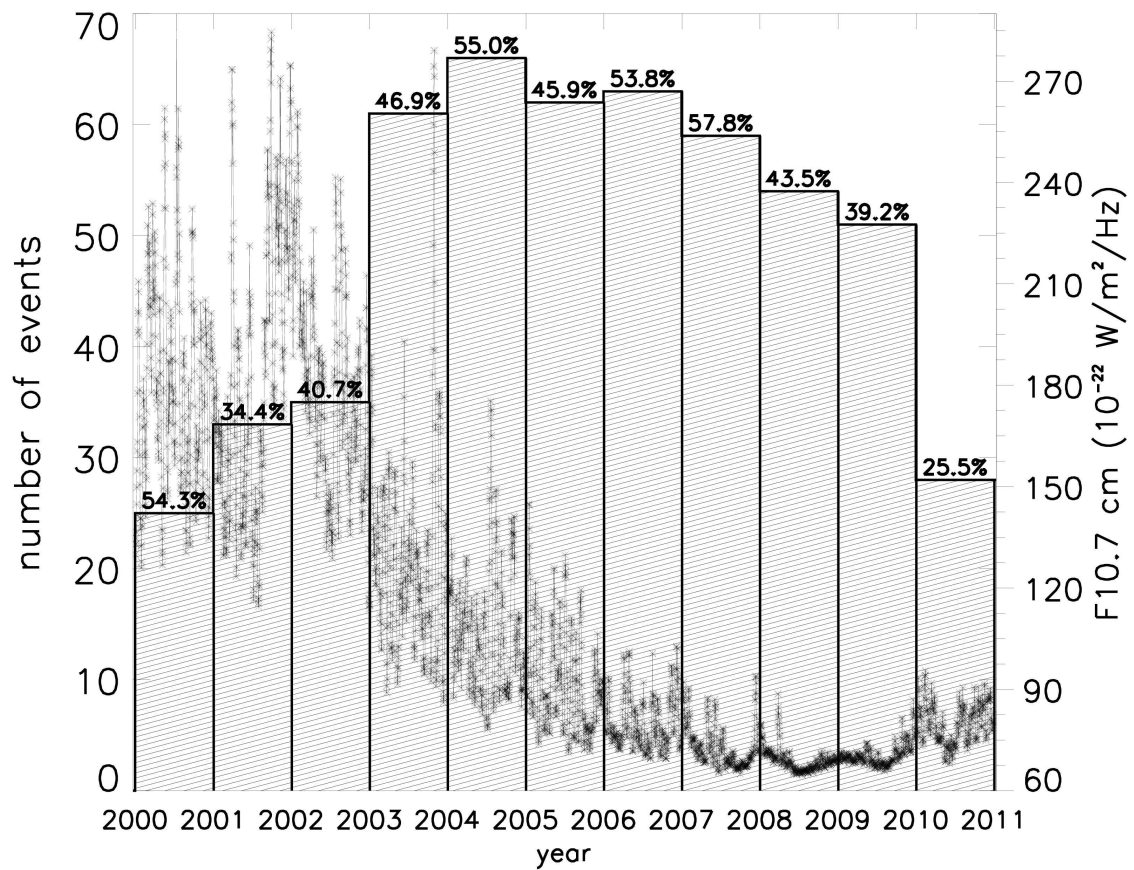


Figura 4.6 - The evolution of the MSGWs according to the solar cycle (i.e. Solar flux F10.7)

Though MLT contains a very small fraction of the total mass, energy and momentum of the atmosphere, it has been recognized that MSGWs in this region is very important driving force for the extratropical middle atmosphere circulation via downward control as reported by ??). They also contributed to the strength of equatorial Quasi Biennial Oscillation (QBO) ?????). However, mesospheric gravity waves fluxes have been reported to be anti-correlated with solar activity levels by ??). This has been investigated by studying the waves and solar cycle activity using solar flux F10.7 as shown in Subseção 4.1.3. It can be observed that the solar cycle activity have no significant effect on the annual night wave events that propagated at the site from year 2000 to 2010. As a result, the lower atmospheric processes are attributed to be the primary concern of meteorology as reported in ??). Thus, the MSGWs in the MLT are under the continuous influence of meteorological effects. These are kinds of physical processes that influence the atmosphere-ionosphere system from below are associated with the lower atmospheric weather. Moreover, ??) related the possible gravity wave sources in the troposphere to meteorological front activities and cloud convections in the low latitude and that meteorological front activities and tropical cloud convections near the equator which also attest the fact that the MSGWs observed in the study area were not influence by space weather events.

Meanwhile, ??) approximated solar activity level by the F10.7 parameter: $F_{10.7} = 80 \times 10^{-22}$ for the low, and $F_{10.7} = 180 \times 10^{-22} Wm^2Hz^{-1}$ for the high insolation flux and considered only GWs with horizontal phase velocities less than $\approx 100ms^{-1}$. They concluded that varying solar radiation flux does not affect the dynamics of GWs directly, but alter the propagation via temperature dependencies of dissipation parameters, static stability, and the background wind. Moreover, ??) discovered that at higher mesospheric levels and in the lower thermosphere, which is at heights of the lower ionosphere, solar EUV and partly X-rays (ionization state) can potentially affect the gravity wave propagation conditions and dissipation. Therefore, the study of the background wind and the temperature will be necessary to study the solar cycle influence.

5 Conclusion and Recommendation

5.1 Conclusion

This project has studied the long term observations of medium-scale gravity waves over Brazilian equatorial region. As part of this objective, 11 years (2000 to 2010) all-sky image measurements of mesospheric gravity waves were made successfully from Sao Joao do Cariri (7.40°S, 36.50°W) of the magnetic equator. The long term observation provided continuous measurements of the medium scale-gravity waves characteristic structures to be analyzed. The characteristics wave events at the site were found to be consistent with prior image measurements from other low latitude sites in Brazil. However, significant differences in the horizontal wavelength at the site indicate the wide range of data sets in long term analysis.

Keograms analysis was used to determine the parameters of 537 medium-scale gravity waves observed in the OH emission at ~87km altitude. These waves were found to be less susceptible to wind filtering effects especially during summer season. It was also observed that some of the medium-scale were capable of propagating into the lower thermosphere where they may have acted directly as seeds for the Rayleigh-Taylor instability development.

The critical layer theory for gravity wave filtering was applied to 2003 dataset to study the effects of middle atmospheric winds on the propagation of medium-scale gravity waves.

The following have been deduced from the results:

- OH NIR airglow images observed by All-sky imager at Cariri are suitable for a good research, as they provide precise information on the directions of phase propagation and the apparent speeds of the waves reaching the upper atmosphere.
- The keogram methodology appear as a good tool to study the spectral characteristics of MSGWs in the MLT;
- The total anisotropy of the propagation direction were preference to Northeast of the site and was more significant during Spring and Summer seasons and autumn and winter were evenly propagated

- The measurements are almost in total agreement between the observed and permitted wave propagation directions and speeds which is in agreement with the previous short term studies in the site.
- It was found that in summer, most of the waves were out of the forbidden region, and propagating northeastward and the waves that fell in the forbidden region might be ducted waves that propagated from a large horizontal distance or doppler shifted outside the forbidden region. It was expected that the critical level might allow the waves to survive within the layer and penetrate into the higher altitudes.
- However, in winter, autumn and spring most of the waves were within the forbidden region and did not survive which makes them unmeasurable or unobservable.
- There was a seasonality in the wave events, for instance, more MSGWs were observed during the Spring and Winter
- The maximum horizontal wavelength, observed period and the phase speed were concentrated between 100 to 150km, 20 to 40m/s and 60 to 80 minutes, respectively
- There is no direct correlation between the solar activity and MSGWs event. Therefore, it can be concluded that, the wave events were primarily generated in Brazil equatorial region by meteorological processes.

5.2 Recommendation

The future study of this work will consider the following;

- The influence of solar activity should be studied in the various meteorological seasons
- Results from other low, medium and high latitude can be combined in the study to enrich the results
- Using ray tracing technique to study the sources of some of the MSGWs
- The study of the background wind and the temperature will be necessary to be considered using observational instruments

- The vertical parameters of the MSGWs can be studied coincidentally using Satellite data

Contracapa